EXPERIMENTS ON THE FACETING AND SUPERSOLIDITY IN HELIUM CRYSTALS
Doctoral Dissertation

Heikki Junes

Helsinki University of Technology
Faculty of Information and Natural Sciences
Low Temperature Laboratory

TKK Dissertations 154
Espoo 2009

EXPERIMENTS ON THE FACETING AND SUPERSOLIDITY IN HELIUM CRYSTALS
Doctoral Dissertation

Heikki Junes

Dissertation for the degree of Doctor of Science in Technology to be presented with due permission of the Faculty of Information and Natural Sciences for public examination and debate in Auditorium AS1 at Helsinki University of Technology (Espoo, Finland) on Friday 20th of February, 2009, at 12 noon.

Helsinki University of Technology
Faculty of Information and Natural Sciences
Low Temperature Laboratory

Teknillinen korkeakoulu
Informaatio- ja luonnontieteiden tiedekunta
Kylmälaboratorio

ABSTRACT OF DOCTORAL DISSERTATION	HELSINKI UNIVERSITY OF TECHNOLOGY P. O. BOX 1000, FI-02015 TKK http://www.tkk.fi

Abstract

This Thesis describes investigations on the solid-liquid interface of helium. Helium crystals represent a unique model system for the studies of the crystalline phenomena, such as faceting and crystal growth, and their surface can be studied, in principle, down to the zero temperature quantum limit ($0\,\mathrm{K} = -273.15°\mathrm{C}$). Helium also becomes extremely pure at low temperatures as all the impurities except the isotopical ones freeze out. In this Thesis the solid-liquid interfaces of both helium-3 and helium-4 have been studied using a Fabry-Pérot interferometer and a high-accuracy pressure gauge.

The optical studies on the faceting of helium-3 crystals have revealed that the quantum motion of the interface, which keeps the solid-liquid interface rough (not faceted) down to 0.1 K, becomes damped at low temperatures. The quantum fluctuations of the interface become more and more damped due to the Fermi-degeneracy of the liquid which creates a bottle-neck for the spin transport through the moving interface. As a result, facets start to appear and, finally, at the lowest temperatures below 0.001 K the solid-liquid interface becomes so localized that it resembles the surface of classical crystals.

The melting curve of high-quality helium-4 crystals has been measured between 0.01–0.32 K with an accuracy of 0.1 Pa without finding any entropy signature which the possible supersolid transition could cause. The entropy below 0.3 K was attributed to phonons in solid and in liquid and the upper limit of the non-phonon entropy was set to $5 \cdot 10^{-8} R$. The measurements on the thermal expansion of liquid helium-4 between 0.02–0.72 K in constant volume pointed out that the rotons start to contribute to the thermodynamics of the solid-liquid interface of helium-4 above 0.3 K. In order to study the role of defects in the possible supersolidity, also the stacking faults were studied on helium-4 crystals.

VÄITÖSKIRJAN TIIVISTELMÄ	TEKNILLINEN KORKEAKOULU
	PL 1000, 02015 TKK
	http://www.tkk.fi

Tekijä   Heikki Junes

Väitöskirjan nimi

Kokeita helium-kiteiden fasetoitumisesta ja suprakiteisyydestä

Käsikirjoituksen päivämäärä 31.10.2008	Korjatun käsikirjoituksen päivämäärä 30.12.2008

Väitöstilaisuuden ajankohta   20.2.2009

☐ Monografia   ☑ Yhdistelmäväitöskirja (yhteenveto + erillisartikkelit)

Tiedekunta	Informaatio- ja luonnontieteiden tiedekunta
Laitos	Kylmälaboratorio
Tutkimusala	Kokeellinen materiaalifysiikka
Vastaväittäjä(t)	Dr. Reyer Jochemsen
Työn valvoja	Prof. Matti Kaivola
Työn ohjaaja	TkT Harry Alles

Tiivistelmä

Väitöskirjassa käsitellään heliumin kide–neste-rajapinnan tutkimuksia. Helium-kiteet edustavat ainutlaatuista mallia kideilmiöiden, kuten fasetoituminen ja kiteenkasvu, tutkimukselle ja niiden kide–neste-rajapintaa voidaan tutkia periaattessa aina nollalämpötilan ($0\,\mathrm{K} = -273.15°\mathrm{C}$) kvanttirajaan saakka. Heliumista tulee myös hyvin puhdasta matalissa lämpötiloissa, kun kaikki epäpuhtaudet isotooppisia lukuunottamatta jäätyvät. Tässä väitöskirjassa on tutkittu sekä helium-3:n että helium-4:n kide–neste-rajapintaa käyttäen Fabry–Pérot-interferometria ja tarkkaa painemittaria.

Helium-3 -kiteiden optiset tutkimukset paljastivat, että kvantittunut pinnan liike, joka pitää kide–neste-rajapinnan karheana 0.1 K saakka, vaimentuu matalissa lämpötiloissa. Pinnan kvanttivärähtelyn vaimeneminen aiheutuu nesteen Fermi-degeneraatiosta, joka muodostaa pullonkaulan atomien spinien kulkeutumiselle liikkuvan pinnan läpi. Sen seurauksena fasetit alkavat ilmestyä kasvavan helium-3 -kiteen pinnalle ja lopulta matalimmissa, alle 0.001 K lämpötiloissa kide–neste-rajapinta paikallistuu niin paljon, että se muistuttaa klassisten kiteiden rajapintaa.

Korkealaatuisten helium-4 -kiteiden sulamiskäyrää mitattiin 0.01–0.32 K lämpötiloissa 0.1 Pa tarkkuudella löytämättä kuitenkaan merkkejä mahdollisen suprakiteisyystransition aiheuttamasta entropiasta. Alle 0.3 K lämpötiloissa entropiat voitiin liittää kiteessä ja nesteessä oleviin fononeihin ja ei-fononisen entropian yläraja voitiin asettaa arvoon $5 \cdot 10^{-8} R$. Nestemäisen helium-4:n lämpölaajenemismittauksista lämpötila-alueella 0.02–0.72 K saatiin selville, että rotonit alkavat osallistua helium-4:n kide–neste-rajapinnan termodynamiikkaan lämpötilan 0.3 K yläpuolella. Hilavirheiden vaikutusta mahdolliseen suprakiteisyyteen tutkittiin tarkastelemalla myös pinousvirheitä helium-4 -kiteissä.

Preface

THIS Thesis would have not been possible without the help of many people who created an inspiring environment to work effectively. Firstly, I am grateful to Mikko Paalanen who has granted me the opportunity to investigate physics at Low Temperature Laboratory.

Secondly, the collaborators in the Interface group have been essential for the success of this work. I would like to thank Harry Alles, who has helped me forward in my scientific endeavor and encouraged me to proceed autonomously. Special thanks go to Igor Todoshchenko, who has always been hard-working and uncompromising what comes to science and has always had the patience to discuss about possibilities in physics. I would like to thank Alexander Parshin, the guru of helium crystals, whose theoretical support has been indispensable for the success of the project. I am also thankful to Viktor Tsepelin, who has built most of the unique experimental equipment and left it in an excellent condition. I should also mention Vesa Vaskelainen, Juho Simpura, Alex Mayorov, Juan Bueno and Matti Manninen, who have contributed to the work presented in this Thesis.

The work in the laboratory would not have been possible without the kind and assiduous support of the laboratory personnel. Very helpful have been the people at workshop for the preparation and at liquefying factory for the running of the experiment. The secretaries have saved a lot of my time from paperwork. I have also benefited a lot from the collaboration with the people in other groups in the laboratory: Rota, YKI, Nano, Pico. Without belittling at any rate, all the colleagues in the lab have been an excellent company during coffee breaks and other recreational moments, always offering opportunities for interesting scientific discussions.

And last but not least, I express my sincere gratitude to my wife and our little son.

List of publications

This Thesis is based on the following original publications, which will be henceforth referred with the respective Roman numeral.

I   I. A. Todoshchenko, H. Alles, H. Junes, A. Ya. Parshin, and V. Tsepelin. *Measurements on the surface tension of ^{3}He crystals near 100 mK.* Journal of Low Temperature Physics **138**, 811 (2005).

II   I. A. Todoshchenko, H. Alles, H. J. Junes, A. Ya. Parshin, and V. Tsepelin. *Faceting of ^{3}He crystals.* Physica B **329-333**, 386 (2003).

III   I. A. Todoshchenko, H. Alles, H. J. Junes, A. Ya. Parshin, and V. Tsepelin. *Surface of a ^{3}He crystal: Crossover from quantum to classical behavior.* Physical Review Letters **93**, 175301/1 (2004).

IV   I. A. Todoshchenko, H. Alles, H. J. Junes, A. Ya. Parshin, and V. Tsepelin. *Growth Dynamics and Faceting of ^{3}He Crystals.* Journal of Low Temperature Physics **148**, 635 (2007).

V   H. J. Junes, H. Alles, A. Ya. Parshin, I. A. Todoshchenko, and V. Tsepelin. *First observation of the critical size of facets on ^{3}He crystals near 1 mK.* Journal of Low Temperature Physics **146**, 85 (2007).

VI   I. A. Todoshchenko, H. Alles, H. J. Junes, and A. Ya. Parshin. *On the growth dynamics of ^{4}He crystals near the first roughening transition.* AIP Conference Proceedings **850**, 337 (2006).

VII   I. A. Todoshchenko, H. Alles, J. Bueno, H. J. Junes, A. Ya. Parshin, and V. Tsepelin. *Melting curve of ^{4}He: No sign of a supersolid transition down to 10 mK.* Physical Review Letters **97**, 165302 (2006).

VIII   I. A. Todoshchenko, H. Alles, H. J. Junes, A. Ya. Parshin, and V. Tsepelin. *Absence of Low-Temperature Anomaly on the Melting Curve of ^{4}He.* Pis'ma v ZhETF **85**, 555 (2007); reprinted in JETP Letters **85**, 454 (2007).

IX   I. A. Todoshchenko, H. Alles, H. J. Junes, M. S. Manninen, A. Ya. Parshin, and V. Tsepelin. *Elementary Excitations in Solid and Liquid ^{4}He at the Melting Pressure.* Journal of Low Temperature Physics **150**, 258 (2008).

X   H. J. Junes, H. Alles, and M. S. Manninen, A. Ya. Parshin, I. A. Todoshchenko. *Stacking Fault Energy in ^{4}He Crystals.* Journal of Low Temperature Physics **153**, 244 (2008).

Author's contribution

My contribution in preparing and running the experiment has been increasing in the course of studies reaching the primary responsibility in the final experiments [**V**, **VIII**, **X**].

In the course of the studies described in this Thesis, my direct input has been decisive mainly in developing the tools to analyze the interferometric images taken on helium crystals [**I**, **II**, **III**, **IV**, **V**, **X**]. I have also contributed in the analysis of the other experimental data [**VI**, **VII**, **VIII**, **IX**]. I have analyzed alone all the data presented in Papers **I**, **V** and **X**, of which I have written Papers **V** and **X**.

In addition, I have built an additional ^{3}He gas handling system and prepared a couple of doubly-winded copper-wire capacitors used to nucleate the crystals. The LabView programs used to record the measurement data and to regulate the temperature in experiments were usually updated by me.

Contents

List of symbols

T_λ	temperature of superfluid transition in ^{4}He
T_F	Fermi temperature of liquid ^{3}He
B	magnetic field strength
T_N	Néel temperature, temperature of magnetic ordering in solid ^{3}He
α	surface tension
g	acceleration of gravity
h	vertical position (or height) of the crystal surface
h_0	reference vertical position of the crystal surface
$\rho_s\ (\rho_l)$	density of solid (liquid)
$\Delta\rho_{sl}$	difference between the densities of liquid and solid
κ_i	principal curvature of the surface
γ_i	surface stiffness component in the direction of the principal curvature
θ	angle between the normals of a facet and a crystal surface
λ	capillary length
p_l	pressure in liquid
p_m	melting pressure
δp	overpressure; excess of the pressure above the melting pressure value
v_R	velocity of rough surface
μ_R	mobility of rough surface
T_R	roughening transition temperature
k_B	Boltzmann's constant
d	height of an elementary step on the facet
V	pinning potential
V_0	unrenormalized value of the pinning potential
γ_0	unrenormalized value of surface stiffness
$k_0\ (k_*)$	short-scale (large-scale) cut-off of surface fluctuations
β	energy of an elementary step on the facet
η	intrinsic damping coefficient of the interface
R_{eq}	equilibrium radius of the facet
R_c	critical radius of curvature of the facet
δp_{thr}	threshold overpressure of crystal growth
$\langle l \rangle$	average distance between the screw dislocations
ξ	width of an elementary step
v	growth velocity of the interface
μ_{st}	step mobility
K	number of steps produced by a single dislocation
v_{st}	step velocity
v_c	critical velocity of steps
c_{mag}	magnon velocity in solid ^{3}He

v_{pb}	pair-breaking velocity in superfluid ^{3}He
J	mass flow onto the interface
$\overline{J}_E$	heat flow through the interface
J_Q	conduction of heat
S_s (S_l)	entropy of solid (liquid)
$\Delta\mu$	chemical potention difference between liquid and solid phases
L	latent heat of solidification
λ	coefficient of latent heat sharing between the liquid and solid
R_K	Kapitza thermal boundary resistance
κ_s (κ_l)	thermal conductivity of solid (liquid)
Z_s (Z_l)	bulk thermal resistance of solid (liquid)
k_{eff}	effective growth coefficient of the rough surface
$\Delta\mu_{\mathrm{mech}}$	mechanical part of the chemical potential difference between liquid and solid phases
k	intrinsic growth coefficient of the rough surface
d_q	distance between two points on the crystal surface
T_{MCM}	temperature of melting curve minimum
R_i	reflectivity of semitransparent mirror i
ϕ	phase of interference
λ_{HeNe}	wavelength of the He-Ne laser light
Δn	difference between the refractive indices of solid and liquid
r	radius of the cylindrically symmetric crystal
k_{st}	growth coefficient of step
$\hbar$	Planck constant
ω_0	high frequency cut-off of surface fluctuations
ν_s (ν_l)	molar volume of solid (liquid)
Θ	Debye temperature
R	gas constant
C_s (C_l)	specific heat of solid (liquid)
c	sound velocity in liquid
n_l	density of atoms in liquid
M_l	molar mass of liquid
U_0	Grüneisen constant
S_{exc}	excess entropy due to superfluid component in solid phase
ρ_{ss}	density of superfluid component in solid phase
Δ	energy of the roton gap
Φ	activation energy of a free vacancy
M^*	effective mass of a free vacancy
m_4	mass of a ^{4}He atom
θ_{tilt}	tilt of stacking fault with respect to vertical plane
θ_L, θ_R	left and right contact angle of the interface to the stacking fault
ϵ_{SF}	energy of a stacking fault

Chapter 1

Introduction

Helium crystals represent a fine model system for the studies of phenomena taking place on a crystal surface such as faceting. In addition to modeling classical properties, Nature has endowed helium with several properties which cannot be studied with ordinary crystals and this renders the study of helium crystals especially intriguing. As the liquid-solid interface of helium exists down to the absolute zero temperature ($T = 0\,\mathrm{K}$), the theories can be tested in the zero temperature quantum limit. Helium is also an extremely pure substance as at low temperatures all impurities except for isotopic ones freeze out.

The small latent heat of crystallization of helium and extremely good thermal conductivity of the surrounding superfluid phase enhance the dynamics of the liquid-solid interface to a level which is so fast that a the melting-freezing wave easily propagates in ^{4}He below $0.5\,\mathrm{K}$ [1]. These crystallization waves have been predicted to propagate also in ^{3}He at temperatures below $0.2\,\mathrm{mK}$ [2]. In ^{3}He the propagation of crystallization waves would be affected by the magnetic field. The lowest temperature to which the liquid-solid interface of ^{3}He has been cooled is, however, $0.35\,\mathrm{mK}$ [3].

Helium crystals can be studied in a relative wide temperature range, which makes it possible to study faceting and crystal growth as a function of temperature. Although helium crystals have been studied already since the discovery of solid helium in 1926 by Keesom [4], there still remains many unanswered questions. Whereas the understanding of the appearance of facets (flat faces) on ^{4}He crystals has been quite well established, the theory of the appearance of facets on ^{3}He crystals has been inadequate [5].

The 1$^{\text{st}}$ part of the Thesis fills this apparent gap in understanding of the roughening of the surface of ^{3}He crystals.

It has been proposed that solid ^{4}He could have a property similar to superfluidity in liquid ^{4}He[6,7]. The possible superflow of vacancies in solid ^{4}He has been investigated by several groups in different experiments before 1990s[8]. In these studies no unambiguous supersolid state was found, but they set the upper limit of $5 \cdot 10^{-6}$ for the possible supersolid fraction in solid ^{4}He and the value of $< 0.5\,\text{nm/s}$ for the critical velocity down to $25\,\text{mK}$. Lengua and Goodkind[9] have observed an increased sound attenuation in the ultrasonic experiments with ultrapure solid ^{4}He. They attributed this observation to the interaction between phonons and vacancies but obtained a higher supersolid fraction $\rho_{\text{ss}}/\rho_s \sim 0.001$ and condensation temperature of $\sim 0.1\,\text{K}$.

In 2004 Kim and Chan revived the interest to a very broad audience to investigate the possible supersolid state of solid ^{4}He by reporting on their torsional oscillator experiments on solid ^{4}He[10,11]. Kim and Chan have observed the so-called non-classical rotational inertia (NCRI) of solid ^{4}He sample which, according to Leggett[12], could be the manifestation of supersolidity. The NCRI, which signified the discovery of the superfluidity of liquid ^{4}He[13,14], is explained by the partial decoupling of the superfluid (supersolid) sample from the rotating container.

It has been originally proposed by Andreev and Lifshitz[15] and Chester[16] that Bose-Einstein condensation of quantum-delocalized point defects could provide the mass flow in the solid. Due to the large zero-point motion of helium atoms, the solid helium at any temperature may contain a finite concentration of zero-point vacancies which would Bose-Einstein condensate at sufficiently low temperatures. Such condensation would result in non-dissipative mass flow in the solid, superfluidity in solid helium, also called as "supersolidity".

Kim and Chan have found that the reduction in the rotational inertia of the cell filled with solid ^{4}He varies from 0.5% to 1.5% depending on the solid density and the purity of ^{4}He[10,11]. They attributed the reduction of the rotational inertia of the cell to the appearance of the supersolid fraction. Rittner and Reppy confirmed the effect and found supersolid signals exceeding even 20%[17]. In addition, they were able with one of their samples to eliminate the signal below the unobservable level by annealing. However, Kim and Chan could not confirm the annealing effect[18]. Different

experiments on the decoupled fraction of solid ^{4}He have shown that the "supersolid" fraction significantly depends on the way the solid ^{4}He is grown, which refers to the involvement of the defects in solid ^{4}He, because the amount of disorder, or, defects (dislocation, grain boundaries, vacancies, impurities) induced in the solid depends on the growth conditions.

Currently, there is a general consensus that the supersolid phenomenon is most probably related to the disorder in solid[19]. Numerical simulations have indeed shown that certain types of defects in solid ^{4}He support mass superflow[20]. If the phenomenon related to NCRI would be an intrinsic property of helium, then it should reveal some excess entropy which could be detected by the measurements of the melting curve. The 2nd part of the Thesis focuses on the search of such entropy signature on the melting curve measured with single high-quality ^{4}He crystals.

In order to understand more the role of disorder in quantum solids, or, quantum defects, it is also necessary to study experimentally single defects and solid samples with well-characterized disorder[21]. The 2nd part of the Thesis also contributes to the study of quantum defects, presenting studies on the stacking faults in solid ^{4}He. Stacking faults, which are planar defects in a single crystal, create canyons on the crystal surface which are similar but shallower than the ones created by grain boundaries.

The experiments described in this Thesis were conducted at the Low Temperature Laboratory (LTL) using the nuclear demagnetization cryostat of the Interface group, which has several cooling stages in order to cool the helium sample down to a temperature below $0.001\,\mathrm{K}$. The windowed experimental cell is located between the half-reflective mirrors of a Fabry-Pérot interferometer. The interferometric images on helium crystals are projected on the sensor of the CCD camera working at around $70\,\mathrm{K}$ inside the vacuum can of the cryostat. From the interferometric images captured by the sensor, the 3D profile of the helium crystals can be reconstructed. A high-resolution capacitive pressure gauge and a low-temperature cold valve enable accurate ($\sim 0.05\,\mathrm{Pa}$) measurements of the pressure of helium.

Organization of this Thesis

This Thesis is organized in the following way. First, in Chapter 1 a general introduction is presented to the studies of the liquid-solid interface of ^{3}He

and ^{4}He. The experimental cell of the Interface group and the interferometric techniques used in imaging helium crystals are described in Chapter 2.

The results of the investigations on the faceting of helium crystals are collated in Chapter 3: the measurements of the surface tension of ^{3}He crystals [**I**], the studies on high-temperature faceting of ^{3}He crystals [**II**], the studies on the roughening of ^{3}He crystals [**III,IV**], the measurements on the collapse of facets on ^{3}He crystals [**V**], and the remarks on the effective crystal growth mode near the roughening transition [**VI**]. The investigations on supersolidity and defects are reviewed in Chapter 4: the measurements of the melting curve of ^{4}He [**VII,VIII,IX**] and of the heat expansion of liquid ^{4}He [**IX**], and the determination of the stacking fault energy in ^{4}He crystals [**X**]. The results and open questions aroused are summarized in Chapter 5.

1.1   Low temperature phase diagrams of ^{3}He and ^{4}He

1.1.1   Thermodynamical phases of helium

Helium has so large zero-point motion of atoms that the wave functions of the atoms significantly overlap and the atoms partly lose their identity and due to that liquid helium exists down to the absolute zero temperature. Helium does not have the triple point where gaseous, liquid and solid phases coexist in equilibrium, but instead, the melting curve is separated from the vapor curve. Helium solidifies only at elevated pressures: ^{4}He at about 2.5 MPa and ^{3}He at 2.9–3.5 MPa. The low-temperature phases of both ^{3}He and ^{4}He, which were studied in Thesis at zero magnetic field, are presented in Fig. 1.1.

Although both the lighter ^{3}He and the heavier ^{4}He isotopes of helium are electrically neutral, their behaviors at the lowest temperatures are very different. In ^{4}He atom both two protons are paired with neutrons, which gives the atom an integer spin and makes it a boson, whereas in ^{3}He atom one of the protons is unpaired, which makes it a fermion. The bosonic ^{4}He liquid becomes superfluid below 2.17 K, whereas the fermionic ^{3}He liquid becomes superfluid at a much lower temperature, below 0.0025 K. The properties of liquid ^{3}He well below its Fermi temperature of $T_F \approx 1$ K resemble the properties of a Fermi degenerate gas[22]. The bosonic ^{4}He has only one
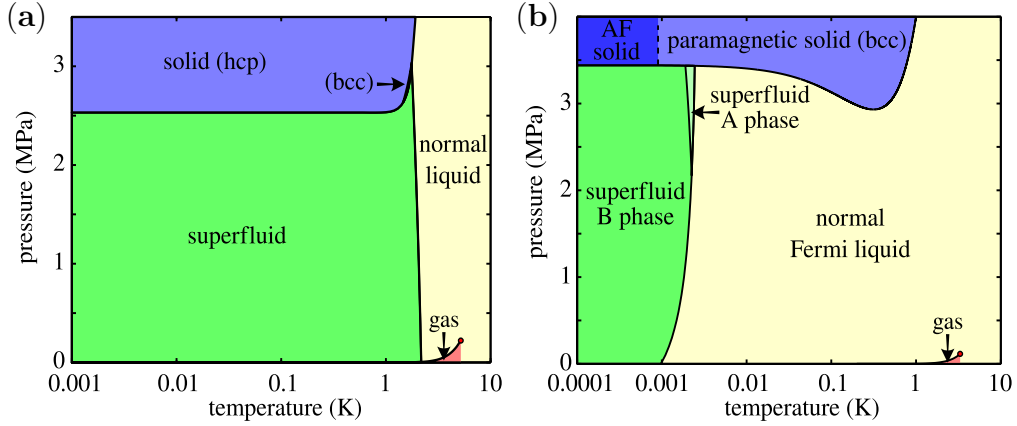
Fig. 1.1   Phase diagrams of (**a**) ^{4}He and (**b**) ^{3}He in zero magnetic field.

superfluid phase, whereas the fermionic ^{3}He has two, superfluid A and B phases in zero magnetic field and also A_1 phase in a magnetic field.

1.1.2   Solid phases of helium

Solid ^{4}He has the hexagonal close-packed (hcp) crystal structure at low temperatures on the melting curve, except between 1.464–1.773 K where the body-centered cubic (bcc) structure is more stable. Due to the hexagonal symmetry, four base vectors are used for classifying the crystallographic planes in the hcp structure, as shown in Fig. 1.2(a). In Figure 1.2(b) are shown several crystallographic planes in the hcp structure.

Solid ^{3}He at low temperatures has body-centered cubic (bcc) crystal structure on the melting curve. Due to the cubic symmetry, the three base vectors used with the bcc structure lie on the x, y and z axes, as shown in Fig. 1.3(a). The ^{3}He atoms have a magnetic moment (spin) and the characteristic spin-spin coupling energy is of the order of the Néel temperature, $T_N = 0.902$ mK. When the temperature of solid ^{3}He is above T_N, the spins in zero magnetic field are disordered and in a finite magnetic field they order paramagnetically. Below T_N, the nuclear spins of solid ^{3}He are ordered into an antiferromagnetic structure shown in Fig. 1.3(b) in which the ferromagnetic (100) planes are believed to order in the sequence of up-up-down-down (u2d2 phase).

(a)

(b)
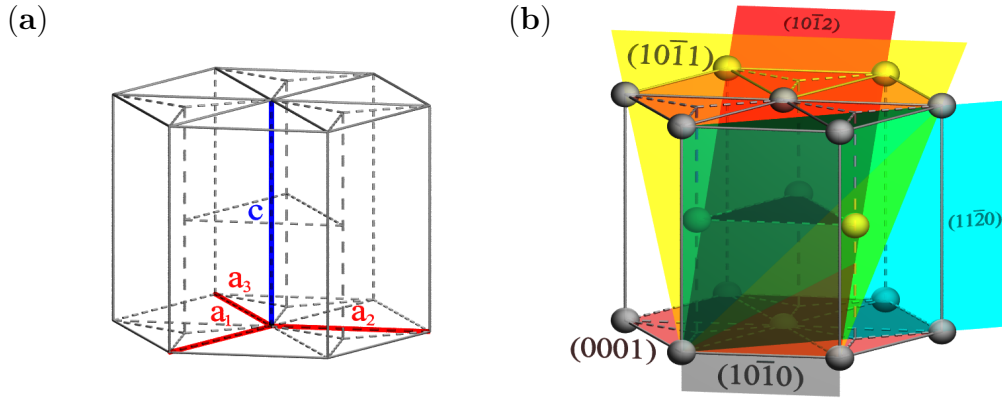
Fig. 1.2   The hcp crystal structure. (**a**) Base vectors $\mathbf{a}_1$, $\mathbf{a}_2$, $\mathbf{a}_3$ and $\mathbf{c}$. (**b**) Plane $(hkil)$ is defined by vectors $\frac{1}{h}\mathbf{a}_1$, $\frac{1}{k}\mathbf{a}_2$, $\frac{1}{i}\mathbf{a}_3$, and $\frac{1}{l}\mathbf{c}$, where $i = -h - k$. In hcp ^{4}He crystals planes $a(10\bar{1}0)$, $c(0001)$ and $s(10\bar{1}0)$ have the largest periodicities in the lattice, $d_a = 0.317$ nm, $d_c = 0.299$ nm and $d_s = 0.280$ nm, then follow planes $(10\bar{1}2)$ with $d = 0.218$ nm and $(11\bar{2}0)$ with $d = 0.183$ nm.

(a)

(b)
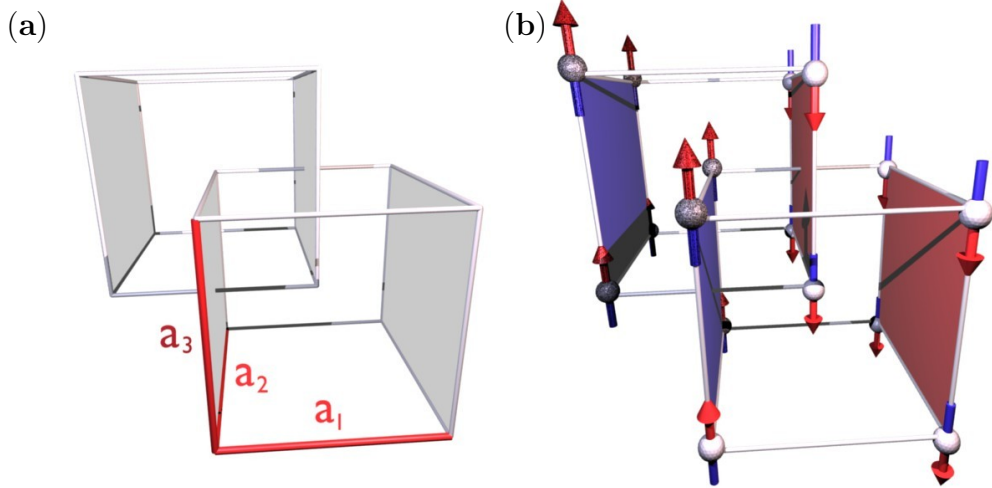
Fig. 1.3   The bcc crystal structure. (**a**) Base vectors $\mathbf{a}_1$, $\mathbf{a}_2$, and $\mathbf{a}_3$. (**b**) The plane (hkl) is defined by vectors $\frac{1}{h}\mathbf{a}_1$, $\frac{1}{k}\mathbf{a}_2$, and $\frac{1}{l}\mathbf{a}_3$. In the magnetically ordered structure of bcc solid ^{3}He the (100) magnetized planes are believed to order in the series of up-up-down-down. In bcc ^{3}He crystals planes (110), (100) and (211) have the largest periodicities in the lattice, $d_{110} = 0.31$ nm, $d_{100} = 0.22$ nm and $d_{211} = 0.18$ nm.

1.2 Liquid-solid interface of helium

1.2.1 Rough crystal surfaces

The equilibrium crystal shape (ECS) is of particular interest in crystallography, because from ECS it is possible to resolve the angular dependence of the surface tension, α. The surface tension measures the work required to increase the surface area by a unit area, or, the force per unit length needed to bend the surface by a unit curvature. According to the Laplace-Young relation,

$$\Delta \rho_{sl} g (h - h_0) = -\alpha \kappa,$$

thus the curvature κ of the surface decreases linearly with the hydrostatic pressure difference $\Delta \rho_{sl} g (h - h_0)$ when vertical position h of the interface changes in the presence of the acceleration of gravity g and the density difference $\Delta \rho_{sl}$ between liquid and solid phases.

In helium crystals the surface tension is in general anisotropic and the Laplace-Young relation has the following form,[23]

$$\Delta \rho_{sl} g (h - h_0) = -(\gamma_1 \kappa_1 + \gamma_2 \kappa_2), \tag{1.1}$$

where for both principal curvatures κ_i of the surface one needs to use the corresponding surface stiffness component γ_i which is related to the surface tension as

$$\gamma_i(\theta_i) = \alpha(\theta_i) + \partial^2 \alpha(\theta_i)/\partial \theta_i^2. \tag{1.2}$$

In case of ^{4}He crystals, the angular dependence of the surface stiffness $\gamma(\theta)$ has been measured by Andreeva and Keshishev[24] from the measurements on the dispersion of the crystallization waves. This anisotropic form (1.1) of ECS has been used in Paper **X** when finding the energy of the stacking fault, although the role of the anisotropy was found to be small.

If the surface tension is isotropic, the surface stiffness equals to the value of the surface stiffness, $\alpha = \gamma_1 = \gamma_2$. This condition holds for a rough, not faceted crystal surface and for a partially faceted crystal surface in orientations which are far from facets. In the isotropic case, the Laplace-Young equation reduces to

$$h - h_0 = -\lambda^2 \kappa, \tag{1.3}$$

where $\lambda = \sqrt{\frac{\gamma}{g \Delta \rho_{sl}}}$ is the capillary length. The capillary length of ^{3}He crystals has been studied at different temperatures in Paper **I**.
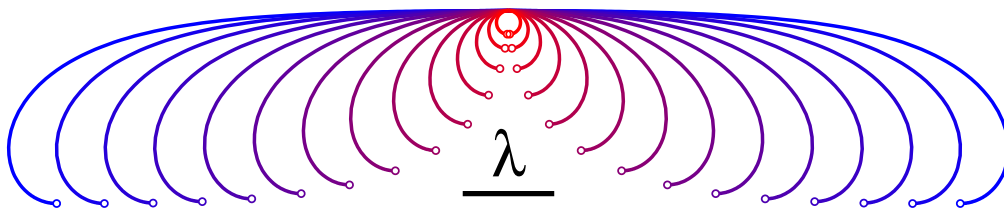
Fig. 1.4 Equilibrium crystal shapes (ECS) in the cylindrical symmetry. Crystals with diameter larger than the capillary length λ flatten out. λ is about 1.0 mm for both ^{3}He and ^{4}He depending slightly on orientation.

Solving numerically equation (1.3) reveals that a rounded crystal whose size is smaller than the capillary length is nearly spherical in the gravitational field, whereas larger crystal flattens out, as shown in Fig. 1.4. If the crystal size increases even more, its height saturates to a value which is a bit larger than 2λ and the top of the crystal becomes nearly flat. Even when the hydrostatic pressure difference across a helium crystal in equilibrium reaches 2–3 Pa, the height change of a large crystal in equilibrium is exponentially small compared to the change of crystal size. This saturation of the crystal height was exploited in Papers **VII**, **VIII** and **IX** when measuring the melting pressure of ^{4}He with high accuracy (~ 0.1 Pa).

If the hydrostatic term and the Laplace term are not balanced, then the liquid pressure p_l is above (or below) the melting pressure p_m and there is an overpressure δp that drives the growth (or melting) of the crystal surface,

$$\delta p = p_l - p_m = -\rho_l g(h - h_0) - \frac{\rho_l}{\Delta \rho_{sl}} \alpha \kappa. \qquad (1.4)$$

Since the growth velocity v_R of rough surface is proportional to the overpressure,

$$v_R = \mu_R \delta p_R, \qquad (1.5)$$

it is possible to determine the effective mobility of the rough surface μ_R by simply measuring the height, velocity and curvature of a rounded surface in several places on the surface. Via relations (1.4) and (1.5) the rounded surface has been used in Papers **III** and **IV**, and **V** as a reference in determining the overpressure on the faceted crystal surface. This method is extremely sensitive (~ 0.01 Pa) and does not require any pressure measurement.

1.2.2 Facets

The interatomic cohesive forces are able to dampen the thermal fluctuations of a crystal surface and at low enough temperature render a rounded (rough) surface into a smooth (flat) one (see Fig. 1.5).

Fisher and Weeks[25] and Jayaprakash *et al.*[26] have found the universal relation between the roughening transition temperature, T_R, the surface stiffnesses, γ_1 and γ_2, and the periodicity d in the lattice,

$$k_B T_R = (2/\pi)\sqrt{\gamma_1\gamma_2}d^2, \tag{1.6}$$

where k_B is Boltzmann's constant. This simple relation predicts the faceting transition for the basal c-facet on ^{4}He crystals to take place at $1.3\,\mathrm{K}$ which agrees with experimental observations but, for the (110) facet on ^{3}He crystals it yields $0.26\,\mathrm{K}$ which is much higher than the highest temperature of $0.10\,\mathrm{K}$ at which facets have been seen[5]. It has been pointed out that the roughening theory which yields relation (1.6) neglects quantum fluctuations of the liquid-solid interface of ^{3}He which are able to roughen the interface[27]. The role of the Fermi degeneracy of liquid ^{3}He in dampening of the quantum fluctuations is studied in Papers **III** and **IV**.

Equation (1.6) can also be used for non-basal facets, but missing accurate data on the surface stiffness of ^{4}He crystals near the facet orientation is not currently available in order to provide accurate predictions[5]. The predictions given by the isotropic surface tension were used in the studies of non-basal faceting on ^{3}He crystals in Paper **II**.
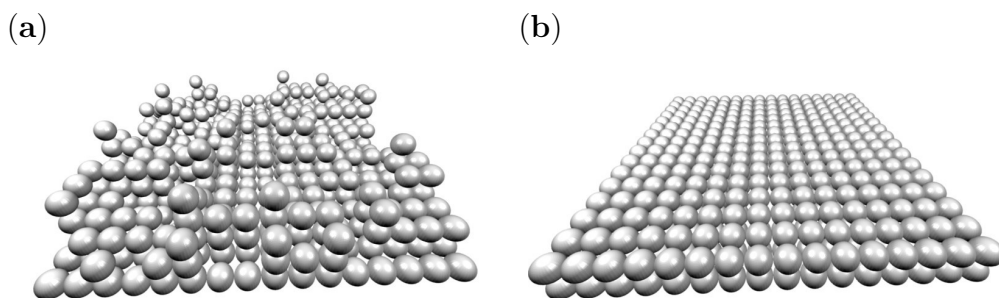
(a)   **(b)**

Fig. 1.5 **(a)** A rough crystal surface. **(b)** A smooth (faceted) crystal surface.

1.2.3   Roughening theory

The roughening of ^{3}He crystals has been studied in Papers **III** and **IV** from the viewpoint of the renormalization theory. In order to compare the roughening of ^{3}He and ^{4}He crystals, it is reasonable to follow Nozières and Gallet[28] who have developed a renormalization group approach for the critical theory of roughening. In the static renormalization group approach, the effective surface Hamiltonian is

$$H = \int \Big[\frac{\gamma}{2}(\nabla z)^2 + V \cos \frac{2\pi z}{d}\Big] d^2 r, \qquad (1.7)$$

where the cohesive forces of the interface, or, the pinning of the liquid-solid interface to the crystal lattice is presented by the periodic potential V which tends to pin the interface at integer positions of z/d. The ratio V/γ describes the strength of the pinning of the interface to the lattice. If V/γ is close to unity then the interface-to-lattice coupling is strong, and if it is small then the coupling is weak.

The pinning potential is the strongest at $0\,\mathrm{K}$. Thermal fluctuations renormalize the pinning potential to a smaller value which weakens the interface-to-lattice coupling, until at the roughening temperature T_R the interface roughens completely. In the weak-coupling limit, $V/\gamma \ll 1$, the renormalization of the surface stiffness γ is negligible at all temperatures except in the narrow temperature region near T_R, $|(T_R - T)/T_R| \lesssim V_0/(\gamma_0 d^2 k_0^2)$. Here are being used the unrenormalized, "bare" values and of the pinning potential V_0 and the surface stiffness γ_0, and the short-scale cut-off $k_0 \sim \pi/d$ of surface fluctuations which are in shorter scale than the periodicity d. The renormalized pinning potential is

$$V = V_0 \exp(-2\pi^2 \langle z^2 \rangle / d^2), \qquad (1.8)$$

where the average amplitude of thermal fluctuations of the interface is

$$\langle z^2 \rangle = (T/2\pi\gamma) \ln k_0/k_*. \qquad (1.9)$$

The large-scale cut-off k_* is at the level when the coupling energy per unit cell, $4\pi V/k^2$, reaches the energy of fluctuations with corresponding k.

The renormalized free energy of an elementary step on a facet is

$$\beta = (4d/\pi)\sqrt{\gamma V}, \qquad (1.10)$$

thus after renormalization the temperature dependent step energy is

$$\beta = \beta_0 \left(\frac{4\pi V_0}{k_0^2 T} \right)^{\frac{T}{2(T_R - T)}},\tag{1.11}$$

where β_0 is the unrenormalized value for the step energy. On ^{4}He crystals the experimental data on the energy of an elementary step β on c-facet has been successfully explained with the renormalization theory[29]. As found in Papers **III** and **IV**, on ^{3}He crystals the step energies β_{110} of the basal (110) facet near $100\,\mathrm{mK}$ can also be explained with the same theory, however, in order to explain the full temperature dependence of β_{110} down to $0.55\,\mathrm{mK}$, the generalized version of the renormalization which includes quantum fluctuations has to be used.

In order to incorporate quantum fluctuations, we used the dynamic version of the renormalization group theory, in which the motion of the interface $z(\vec{r}, t)$ is described with the Langevin-type equation,

$$\eta \frac{\partial z}{\partial t} - \gamma \nabla^2 z + (2\pi V/d) \sin(2\pi z/d) = R(\vec{r}, t),\tag{1.12}$$

where η is the intrinsic damping coefficient of the interface and $R(t, \vec{r})$ is the time-dependent random force. In the case of thermal fluctuations the random force has white spectrum,

$$R_{k,\omega}^2 = 2\eta \, T \, f(k) \, g(\omega),\tag{1.13}$$

where f and g are the form factors used to cut off the renormalization, $f(k) = \theta(1 - k/k_0)$ and $g(\omega) = \theta(1 - \omega/\omega_0)$, where $\theta(x)$ is the step function. In order to describe also quantum fluctuations of the interface, the random force has to be replaced with its general form,

$$R_{k,\omega}^2 = 2\eta \, \hbar\omega \, \coth \frac{\hbar}{2k_B T} \, f(k) \, g(\omega).\tag{1.14}$$

The static and dynamic renormalization theories yield the same results at the roughening transition temperature T_R where thermal fluctuations dominate. In Papers **III** and **IV** it indeed has been found that the generalized renormalization group theory is able to explain the renormalization of the step energy β_{110} in ^{3}He crystals in full temperature range from $0.55\,\mathrm{mK}$ to $103\,\mathrm{mK}$.

1.2.4   Equilibrium and critical size of facets

The shape which crystals tends to take has been already in 1885 considered by P. Curie, who stated that the crystal surface should take such a form which minimizes its surface energy[30]. He also noticed that the surface tension α has a minimum in the direction of flat facets and that the minimum in α is responsible for the finite-size facets. Later, in 1901, Wulff proved that the distance from the origin of the crystal to the facet is proportional to the surface tension of the facet[30]. About 50 years later, Landau has shown that the derivative of the surface tension $\partial\alpha/\partial\theta$ has a jump at the orientation of the facet which is proportional to the step energy β. Following the approach developed by Wulff, Landau has found that the equilibrium size of the facet is proportional to the value of the jump, or, to the step energy,

$$\frac{R_{\mathrm{eq}}}{L} \propto \frac{\beta/d}{\alpha},\tag{1.15}$$

where L is the characteristic size of the crystal.

In the faceting–roughening problem, the step energy β is the order parameter that describes the strength of the coupling between the crystal surface and the lattice. This can easily be seen from equation (1.15)—if β is finite, facets should appear on the crystal surface. If the ratio $\frac{\beta/d}{\alpha}$ is close to unity, then the equilibrium facet size is of the order of the crystal size and the surface-to-lattice coupling is said to be strong. If $\frac{\beta/d}{\alpha}$ is small, the equilibrium facet size is much smaller than the crystal size and the coupling is said to be weak. For zero step energy also the equilibrium facet size is zero.

By measuring the equilibrium size R_{eq} of a facet one could, in principle, obtain the value of β. The difficulty of this method, however, has been that the relaxation time of a faceted crystal has not been experimentally accessible, due to the thresholds which exist in the facet growth (see next section). In the case of ^{3}He at high temperatures, also the large latent heat of crystallization and poor thermal conductivity of the normal liquid increase the relaxation times of crystals.

There are, however, other methods with which the step energy of facets can be measured under quasi-equilibrium conditions. As suggested by Marchenko and Parshin[31], the step energy of the basal c-facet on ^{4}He crystals has been measured by studying the surface-to-wall contact angle as a function of the angle between the facet and the wall[32]. Another way is to follow the shape of faceted crystals during slow melting and, at the

moment when the facets collapse, measure the critical size of facets,[23]

$$R_c = \frac{\rho_l}{\Delta\rho_{sl}}\frac{\beta}{d\,\delta p},\tag{1.16}$$

which equals to a half of the equilibrium size R_{eq} of facets. The step energies of the (110) and (100) facets on ^{3}He crystals near $1\,$mK have been determined in Paper **V** by measuring the critical size R_c and the overpressure δp of collapsing facets.

1.2.5   Growth modes of facets

A faceted crystal surface may grow through the appearance of new atomic layers on the surface. New atomic layers can be created by the 2D nucleation or by the spiral growth through screw dislocations. Compared to the growth of the rough surface which is linear to the driving overpressure δp, it is characteristic to a faceted surface that its growth below T_R is non-linear to δp. Only above T_R, where the facet roughens, the growth in the direction of a facet becomes linear to δp.

In the 2D nucleation of new layers of atoms there is a threshold which has to be overcome. In order for a terrace of a new layer to expand, its size has to exceed the critical size given in equation (1.16). The growth through a single screw dislocation does not include a threshold. However, neighboring screw dislocations of opposite windings form a pair which is called a Frank-Read source[33]. The Frank-Read sources have a growth threshold of

$$\delta p_{\mathrm{thr}} = 2\beta/d\langle l\rangle,$$

where $\langle l\rangle$ is the average distance between the screw dislocations. Since the growth threshold in spiral growth is typically smaller than in the 2D nucleation of new layers, 2D nucleation is effective only close to T_R where the step energy β is very small and the critical size of the facet becomes smaller than the size of Frank-Read sources, $R_c < \langle l\rangle/2$. On the other hand, the critical theory of roughening predicts also that the step width ξ increases with the decreasing step energy,[23]

$$(\xi/d) = \frac{2}{\pi^2}\frac{\gamma d}{\beta}.\tag{1.17}$$

As found in Paper **VI** for ^{4}He crystals, this broadening of the step near T_R may again make the spiral growth more effective than the 2D nucleation.

The step energy β can be determined from the crystal growth through screw dislocations by measuring the quadratic dependence of the growth velocity v on the overpressure δp [34],

$$v = \frac{\mu_{\text{st}}\, d^3}{19\,\beta} K \left(\frac{\Delta\rho_{sl}}{\rho_l}\right)^2 (\delta p)^2. \tag{1.18}$$

Here μ_{st} is the step mobility and K is the number of steps produced by one dislocation. In Papers **III** and **IV** the quadratic dependence of the facet velocity to δp was found out to determine the step energy of the (110) facet.

On ^{3}He crystals at low temperatures the step velocity v_{st} reaches already at an overpressure of $\delta p_{\text{thr}} \approx 5\,\text{Pa}$ the critical velocity $v_c = 7\,\text{cm/s}$, which is close to the magnon velocity c_{mag} in the solid ^{3}He and pair-breaking velocity v_{pb} in superfluid ^{3}He. After reaching this critical velocity the step mobility becomes suppressed and the growth velocity of facet becomes linear to δp [34],

$$v = \frac{v_c\, d^2}{2\pi\beta} K \left(\frac{\Delta\rho_{sl}}{\rho_l}\right) \delta p. \tag{1.19}$$

In Paper **V**, the step having width ξ has been considered as a rough surface tilted by (d/ξ), which yields a lower estimate for the mobility of the rough surface, $\mu_R = (\xi/d)(v_c/\delta p_{\text{thr}})$.

In the absence of screw dislocations or when the growth threshold of a facet is very high, new atomic layers may be nucleated at the contact of the facet to the wall [5]. As realized by Marchenko and Parshin, it is possible that the contact of the surface to the wall becomes a source of new atomic layers for the immobile facet [31]—the threshold of the c-facet growth on ^{4}He crystals has been observed to vanish when the facet-to-wall contact angle decreases below $\sim 47°$ [32], which has been also indirectly observed in Paper **X**.

In experiments with ^{4}He crystals there has been observed also a very fast growth mode, which have not been completely understood yet. Parshin *et al.* have seen "avalanche-like" growth of vertical c-facets [35] and Ruutu *et al.* [36] have seen "burst-like" growth of new atomic layers for c-facets which are oriented horizontally. The burst-like growth proceeds stochastically, with overpressures ranging from about 10 to $100\,\text{Pa}$ at $T = 200\,\text{mK}$. The role of the creation of stacking faults in these fast growth modes is discussed in Paper **X**.

1.2.6   Heat considerations on the growth of crystals

The movement of a liquid-solid interface is accompanied by the release of latent heat of crystallization and the transport of the released heat through the interface and through bulk phases. Nozières and Uwaha[37] have found the coupling between the mass flow $J = v\rho_s$ and heat flow $\overline{J}_E$. The heat flow through the interface, $\overline{J}_E = J_Q + TSJ$, has two terms which describe the conduction of heat, $J_Q = \kappa\nabla T$, and the convection of heat, TSJ. Then the coupling of the mass and heat flows across the interface can be written with a paired equations

$$J = k\big[\Delta\mu + \lambda\frac{\Delta T}{T}\big] \tag{1.20}$$

$$\Delta T = R_K[\overline{J}_E - \lambda J], \tag{1.21}$$

in which k is the isothermal growth coefficient, $\Delta\mu = \mu_l - \mu_s$ is the chemical potential difference over the interface, R_K is the Kapitza thermal boundary resistance of the interface, and the term λ describes the share of the latent heat $J(S_l - S_s)T$ between the liquid side, $J(TS_l - \lambda)$, and the solid side, $J(\lambda - TS_s)$. The temperature difference ΔT across the interface can be written in a symmetric form

$$\Delta T = R_K[\kappa_l\nabla T_l + J(TS_l - \lambda)] = R_K[\kappa_s\nabla T_s + J(TS_s - \lambda)]. \tag{1.22}$$

The heat release at the moving interface is depicted in Fig. 1.6 which shows how the heat is elaborated on both sides of the interface and conducted both through the bulk thermal resistance Z_l and Z_s and through the Kapitza thermal boundary resistance R_K[37]. In solving the heat diffusion problem for a facet and for a rough surface in Papers **III** and **IV**, equation (1.22) was used as one of the boundary conditions.

When a rough crystal surface is growing, the velocity of the moving interface is proportional to the overpressure that drives the crystal growth. Experimentally measurable quantity is the effective growth coefficient $k_{\text{eff}} = \frac{J}{\Delta\mu_{\text{mech}}}$
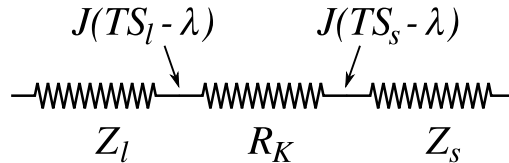

Fig. 1.6   Thermal circuitry across the moving interface.

which is defined using the *mechanical* part of the chemical potential difference between liquid and solid $\Delta\mu_{\text{mech}} = \frac{\Delta\rho_{sl}}{\rho_l\rho_s}\delta p$,

$$1/k_{\text{eff}} = 1/k + \rho_s \left[\frac{R_K Z_l (TS_l - \lambda)^2 + R_K Z_s (TS_s - \lambda)^2 + Z_l Z_s L^2}{T(R_K + Z_l + Z_s)} \right]. \quad (1.23)$$

In general case k_{eff} includes the elaboration and transport of heat and therefore the value of k_{eff} depends on what thermal impedances contribute to the measurement of $\Delta\mu_{\text{mech}}$. In previous experiments[38,39,40,41] the effective growth coefficient has corresponded to the thermal impedance of the liquid between the crystal surface and the sinter, including the sinter. In contrast, the effective growth coefficients measured in this Thesis correspond to the thermal impedance between different parts of the surface and can be therefore called as *differential* growth coefficients.

Equation (1.23) simplifies in the case of ^{3}He crystals below about $1\,\text{mK}$ where the thermal impedance of liquid is much smaller than that of solid, $Z_l \ll Z_s$, the Kapitza resistance is negligible[42], $R_K \ll Z_l$. Then the growth of the rough surface is limited by the latent heat transport,

$$1/k_{\text{eff}} = \rho_s \frac{Z_l L^2}{T}, \quad (1.24)$$

and there is no matter how the latent heat is shared between liquid and solid phases. This temperature scaling of k_{eff} was used in Paper **V** when estimating the overpressure on the growing rough surface.

Another limit of equation (1.23) is obtained for ^{3}He crystals at high temperatures where the latent heat is elaborated in the liquid side[43,44], $\lambda = TS_s$. Solid ^{3}He which conducts heat better than liquid ^{3}He, $Z_s \ll Z_l$, acts as a short-cut for the transport of heat between the different surface parts. Due to the short-cut in transporting heat between two points separated by a distance d_q on the crystal surface, the Kapitza resistance R_K does not scale with distance, whereas the thermal impedance of the liquid Z_l scales with d_q. In large scales, $d_q \gg R_K \kappa_L \approx 10\,\mu\text{m}$, Kapitza resistance becomes small compared to the liquid impedance, $R_K \ll Z_l$. Then the growth of the rough surface is limited by the latent heat transport through the interface,

$$1/k_{\text{eff}} = \rho_s \frac{R_K L^2}{T}. \quad (1.25)$$

This temperature scaling of k_{eff} has been used in Papers **III** and **IV**.

Chapter 2

Experimental techniques

2.1   Experimental cell

The experimental cell of the Interface group is made of copper, it has cylindrical experimental volume and optical windows through which the helium sample can be imaged. The windowed experimental cell is located between two half-reflective mirrors which form a Fabry-Pérot interferometer. A photograph of the experimental setup is shown in Fig. 2.1.

Helium is injected to the experimental cell through a filling line which goes all the way from room temperature down to the cell at low temperatures. The filling line is thermally anchored to each cooling stage. A cryogenic valve anchored to the mixing chamber of the dilution refrigerator isolates the cell from thermoacoustic (Taconis) oscillations in the filling line.

Solid helium nucleates spontaneously when the pressure of liquid helium exceeds the melting pressure by about $1\,\mathrm{kPa}$. The overpressure needed to nucleate a seed of crystal can be lowered with a nucleator, which in our case is a bifilar coil wounded around a bakelite holder. When a high voltage of about 300–$700\,\mathrm{V}$ is applied over the coil of the nucleator, the electric field produced permits a seed of crystal to nucleate at an overpressure of $0.4\,\mathrm{kPa}$ or less. The growing seed initially hangs on the coil of the nucleator. When the size of the crystal is large enough, the crystal drops on the bottom window of the experimental cell.
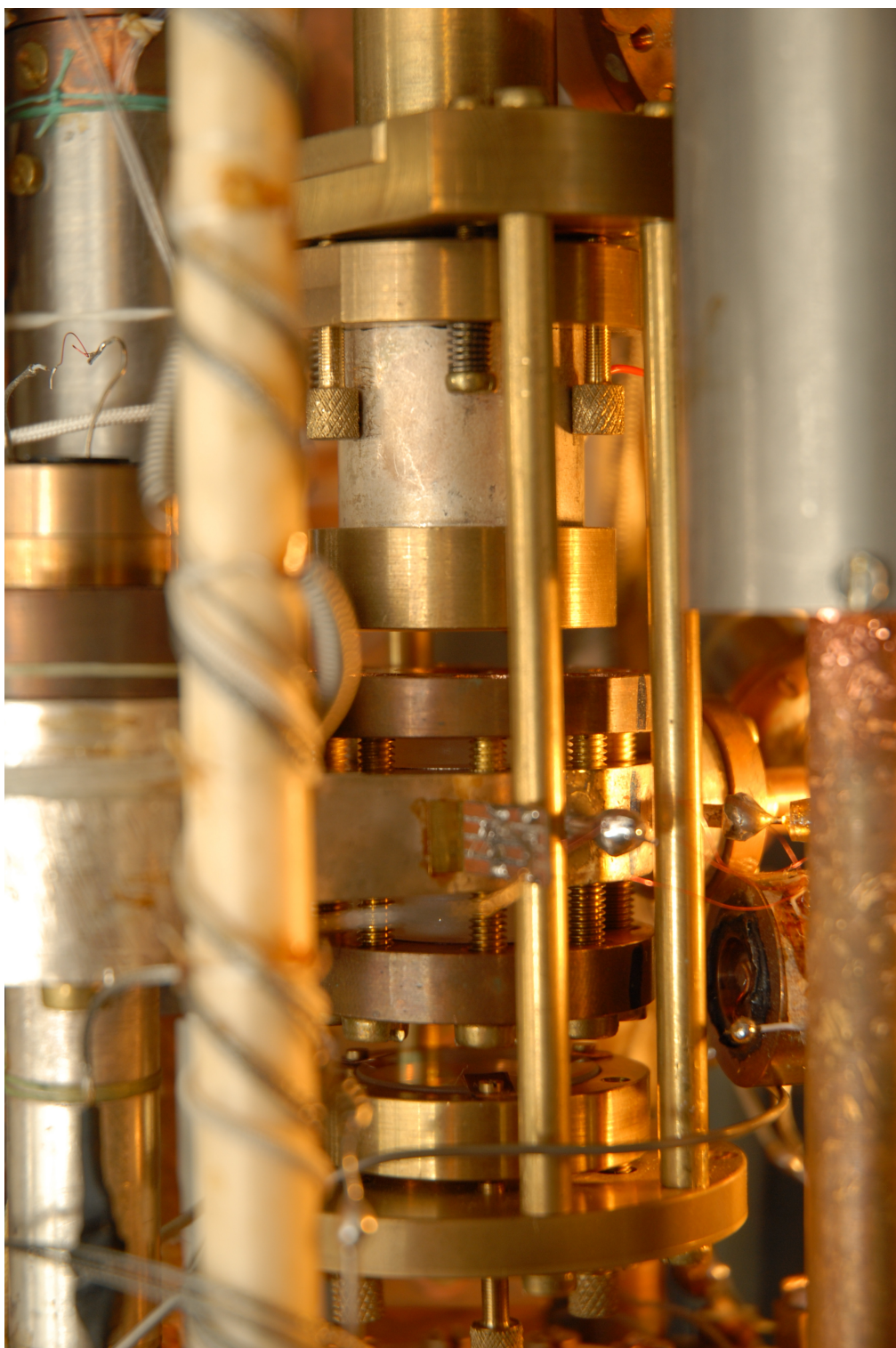
Fig. 2.1   Photograph of the experimental setup of the Interface cryostat.
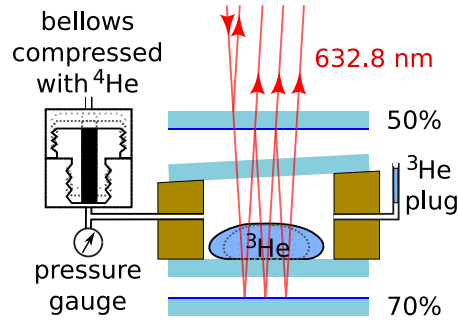
Fig. 2.2 A ^{3}He crystal in the isolated cell can be grown by increasing the pressure of ^{4}He in the bellows which compress the cell volume.

When pressurizing ^{3}He at a low temperature through the filling line, a crystal nucleates first at $T_{\mathrm{MCM}} = 315\,\mathrm{mK}$ in the filling line due to the large depth $(0.6\,\mathrm{MPa})$ of the melting curve minimum of ^{3}He. That crystal grows and forms a plug which isolates the experimental cell from further pressurizing through the filling line. In order to overcome this problem Pomeranchuk type compressional cell is typically used. In the Interface cryostat the flexible part of the experimental cell consists of compressible bellows, as schematically shown in Fig. 2.2. The compressing of the bellows with ^{4}He decreases the experimental volume and increases the pressure of ^{3}He in the cell.

In the case of ^{4}He the depth of the melting curve minimum is only $0.8\,\mathrm{kPa}$, which is below the spontaneous nucleating overpressure of a ^{4}He crystal. The shallow minimum enables pressurizing the cell directly through the filling line, as schematically shown in Fig. 2.3. However, in order to ensure the nucleating of a ^{4}He crystal in the cell, it is necessary to use nucleator in the same manner than with ^{3}He crystals.
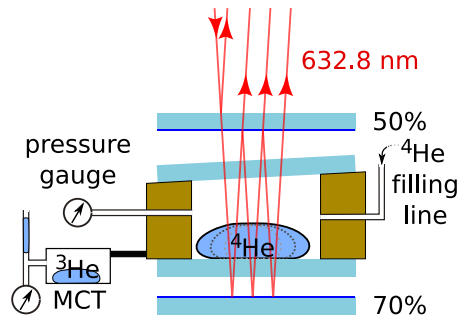

Fig. 2.3 A ^{4}He crystal can be grown by injecting ^{4}He through the filling line. An accurate ^{3}He melting curve thermometer is thermally linked to the cell body.

The pressure of liquid helium is measured using a capacitive pressure gauge. In the experiments on ^{3}He crystals, the liquid pressure on the melting curve was also used for thermometry. In ^{4}He experiments, a separate ^{3}He melting-curve thermometer (MCT) was thermally anchored to the experimental cell, as shown in Fig. 2.3. The melting pressure of ^{3}He is generally accepted as a provisional low temperature scale, PLTS-2000, between $T_N = 0.902\,\mathrm{mK}$ and $1\,\mathrm{K}$.[45] Below T_N, the nuclear ordering temperature of bulk solid ^{3}He, we used the T^4-law due to magnons in solid ^{3}He to connect the pressure at T_N to the pressure at $0\,\mathrm{K}$, $P(0\,\mathrm{K}) - P(T_N) = 198.7\,\mathrm{Pa}$,[46] obtaining thus relation $P(T) - P(T_N) = 198.7\,\mathrm{Pa}\,[1 - (T/0.902\ \mathrm{mK})^4]$. [1]

2.2   Optics and interferometry

2.2.1   Optical setup

The helium crystals are illuminated with the light from a $5\,\mathrm{mW}$ He-Ne single-mode laser working at room temperature. The light of the laser is guided to the cryostat through an optical single-mode fiber. At the end of the fiber there is a beam expander which diverges the light to propagate radially. The radial beam is rectified by a converging lens. The planar light encounters first a beam splitter which is a semitransparent mirror. The reflected part of the light proceeds towards the cell and the transmitted part of the light ends up to the light absorber behind the beam splitter.

The windowed cell is located between two semitransparent mirrors which form the Fabry-Pèrot interferometer. The planar light which encounters the two semitransparent mirrors perform one or more reflections, as shown in Figs. 2.2 and 2.3. The reflected light beams then pass through the beam splitter, three lenses which adjust the beam size, two mirrors forming a periscope, and an infrared filter before interfering on the sensor of the CCD camera. The infrared filter and the periscope prevent the infrared radiation of the camera working at $60\,\mathrm{K}$ from warming the helium sample in the cell. Helium crystal has a larger optical density than helium liquid and, as a result, the interference pattern on liquid helium is modulated by the thickness of a helium crystal.

---

[1]In Paper **V**, the exponent 4 in term $(T/\mathrm{mK})^4$ has been erroneously changed into a citation to[45].
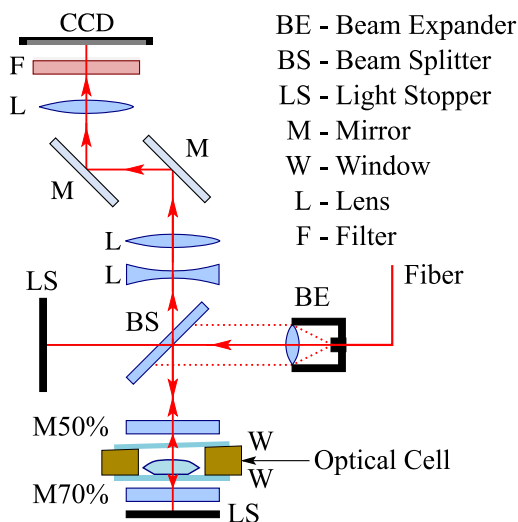
Fig. 2.4   The optical setup inside the Interface cryostat.

The images of helium crystals taken with our Fabry-Pèrot interferometer provide 3D thickness plots. In low temperature imaging it is crucial to have such an optical setup that the effects that could possibly warm the sample are minimized. In the optical setup of the Interface cryostat shown in Fig. 2.4, there are no direct optical paths to the experimental cell which could pass infrared radiation to directly heat the helium sample.

2.2.2   Interference pattern

The interference pattern produced by the Fabry-Pérot interferometer, which is a multiple-beam interferometer, is not sinusoidal like in the case of the two-beam interferometry. With carefully chosen reflectivities R_1 and R_2 of the semitransparent mirrors it is possible to tune the fringe pattern $I(\mathrm{x})$ to have either wider minima or wider maxima for the same intensity pattern $I_0(\mathrm{x})$ and phase pattern $\varphi(\mathrm{x})$,[47]

$$I(\mathrm{x}) = I_0(\mathrm{x}) \frac{R_1 + R_2 - 2\sqrt{R_1 + R_2}\cos\varphi(\mathrm{x})}{1 + R_1 R_2 - 2\sqrt{R_1 + R_2}\cos\varphi(\mathrm{x})}. \tag{2.1}$$

In practice, the fringe shape depends not only on the reflectivities of the mirrors but also, e.g., on the slight nonparallelity of the mirrors which distorts the symmetry of the interference pattern[48], on the number of

reflections which depends on the local intensity of the light, and optical defects like dust particles. A helium crystal which is convex in its shape acts also as a converging lens producing a lens effect that slightly refracts the interfering beams creating secondary ripples in the interference pattern. The interference pattern read with the CCD sensor at 60–70 K is also slightly blurred due to the charge carrier freeze-out ($k_B T = 5 - 6\,\text{meV} < E_{\text{ionization}}^{\text{donor}} = 39 - 54\,\text{meV}$) that causes local trapping of the charge carriers and the varying of the charge transfer efficiency with the signal level (i.e., CTE hysteresis)[49]. The areas in which the fringe shape is significantly distorted are typically avoided in the analysis of the interference pattern.

2.2.3 Solving the phase of interference

The phase of interference at each pixel is mapped onto the interference pattern by the fringe profile. In earlier experiments by the Interface group this phase has been directly found out at each pixel with the $\pi/2$ phase-shift technique which employs a piezo-drive to vary the distance between the half-reflective mirrors of the interferometer[50]. The $\pi/2$ phase-shift technique needs however four images to be taken and it is therefore slow and applicable only in situations where the dynamics of the crystal is slow and the crystal shape does not noticeably change in about 10 s, which is the time required to take four images with our slow-scan camera. With fast growing crystals the phase of interference has to be found out from a single frame. Although the exposure time of the CCD is only 0.1 s, subsequent images can be taken every 3–4 s which is the scanning time of the sensor.

If the crystal thickness changes in a known way, for instance linearly as in the case of facets (see Fig. 2.5) or following ECS in the case of rough surface (see Fig. 1.4) the whole area of interest can be fitted with a single function which maps the crystal thickness with the fringe pattern. In other cases it is necessary to solve the inverse problem, in which the phase of the interference is found out at each pixel of the CCD sensor. If the phase changes slowly within the area of interest, it is possible to select a $N \times N$ area around each pixel and to solve the phase in each area. Although the interference pattern is not sinusoidal, it is reasonable to approximate the fringe pattern in the fitting area with sinusoidal washboard function. The initial parameters of the fit, namely the phase, density and direction of the fringes can be found with two dimensional Fourier Transform (FT) applied on the area.
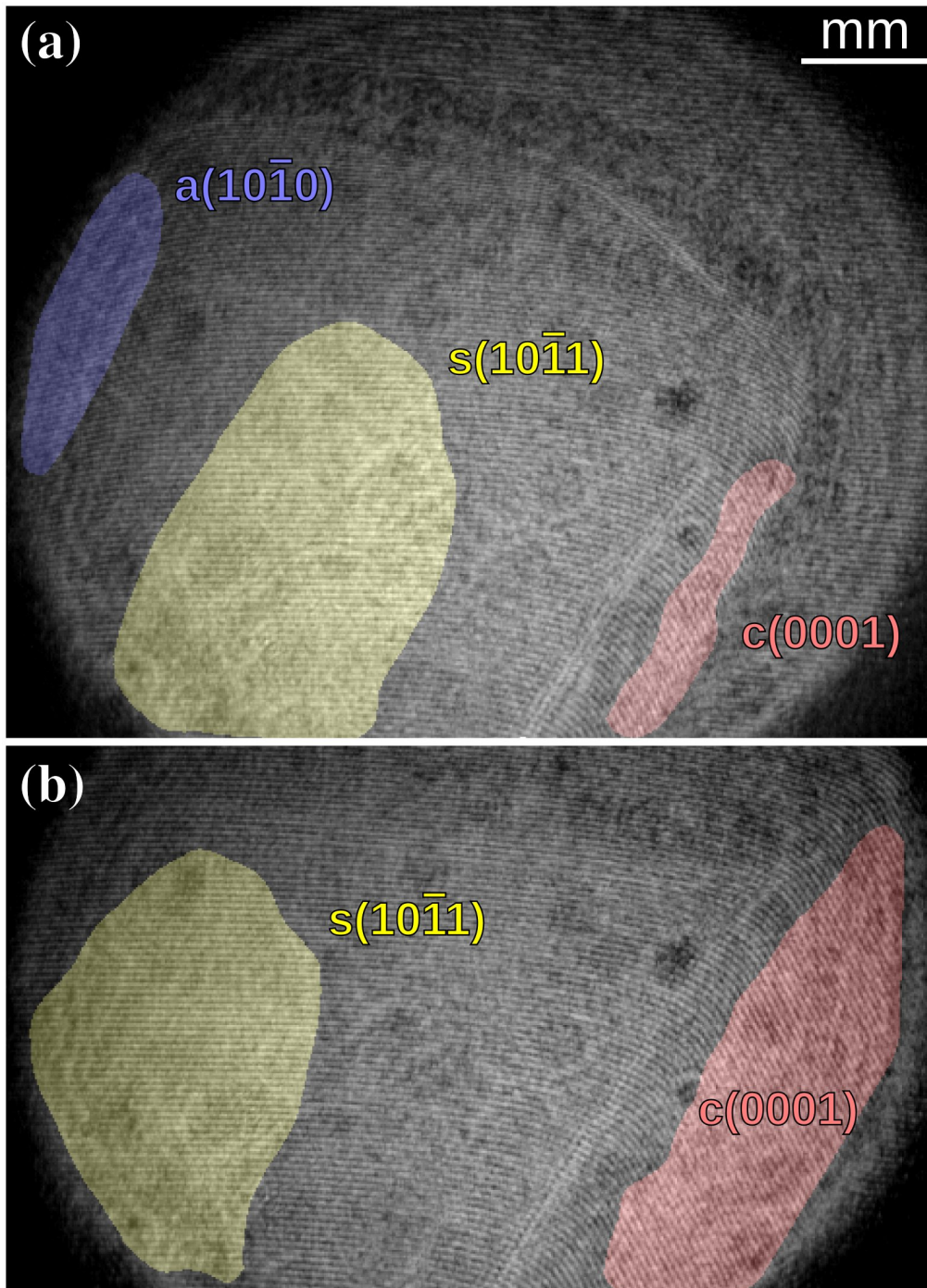
Fig. 2.5 Interferogram of a growing ^{4}He crystal (**a**) at $0.45\,$K and (**b**) at $0.50\,$K. *Highlighted areas* enclose the *c*-facet, *a*-facet, and *s*-facet. The faceted areas have been colored with the Chirp z-transform (CZT) applied on the 41×41 areas around each pixel (see text). Previously the highest temperature of observation of the *s*-facet was a bit lower, $0.43\,$K$^{[51]}$.
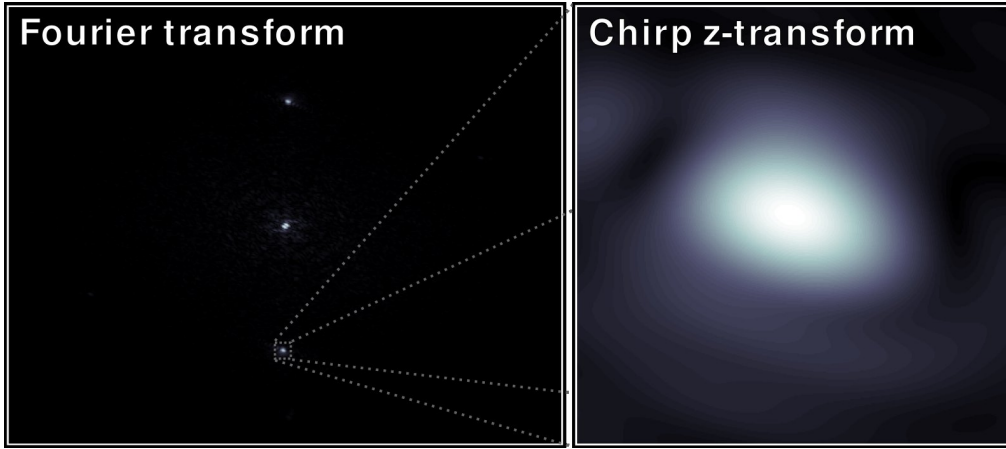
Fig. 2.6 Fourier transform and Chirp z-transform in two dimensions of the interference pattern of the *s*-facet area shown in Fig. 2.5(a).

If only an approximate solution is needed, the fringe density and the phase given by FT can be used for a single area. More accurate solutions can be found out by applying the Chirp z-transformation (CZT) which generalizes FT. Whereas FT is used to solve all harmonics within the area, with CZT it is possible to focus only to a certain set of harmonics and even to zoom into the wave vectors between the main harmonics of FT, as shown in Fig. 2.6. CZT has been used to mark the positions of the *c*-, *a*-, and *s*-facets in Fig. 2.5.

The phase of interference does not however give directly the thickness profile since it is 2π wrapped. The continuous phase can be found out by unwrapping the phase. Once the continuous phase φ has been found out, the thickness of the crystal can be established as $(\lambda_{\mathrm{HeNe}}/4\pi\Delta n)\varphi$, where $\lambda_{\mathrm{HeNe}} = 632.8\,\mathrm{nm}$ is the wavelength of the He-Ne laser light and Δn is the difference between the refractive indices of solid and liquid helium. One notable thing is that the same optical setup can been used in the studies of both ^{3}He and ^{4}He crystals, since the only parameter which changes is Δn, which in the low-temperature limit is $1.66 \cdot 10^{-3}$ for ^{3}He and $3.6 \cdot 10^{-3}$ for ^{4}He. Thus, the change of 2π in phase corresponds to the change of $0.19\,\mathrm{mm}$ of the crystal thickness in ^{3}He and $0.09\,\mathrm{mm}$ in ^{4}He.

Chapter 3

Studies on the faceting and roughening of helium crystals

3.1   Rounded crystals

There has been a puzzle for a long time that why the roughening transition in ^{3}He crystals given by the universal relation (1.6) is 260 mK, whereas facets have been seen only below 100 mK [27]. As the roughening transition temperature is proportional to the surface tension value, one possible reason for the discrepancy could be that the surface tension would be temperature dependent, which would lower the highest temperature where facets could be observed.

Between 140 and 330 mK Rolley et al. [27] have measured for ^{3}He crystals the value of the surface tension $\alpha = 0.060 \pm 0.011 \, \mathrm{mJ/m}^2$. In this Thesis work, the surface tension α has been determined in Paper **I** for ^{3}He crystals at lower temperatures, between 77 mK and 110 mK. Although facets should be present on ^{3}He crystals below 0.1 K, the step energy for the (110) facet at these temperatures is still small and, as a result, the shape of the crystal after slow melting appears to be close to the cylindrical symmetry, as can be seen in Fig. 3.1.

For a rounded crystal (with rough surface) which lies on a horizontal substrate, ECS in gravitational field is cylindrically symmetric. Laplace-Young equation (1.3), which describes ECS, can be reduced into the cylindrically
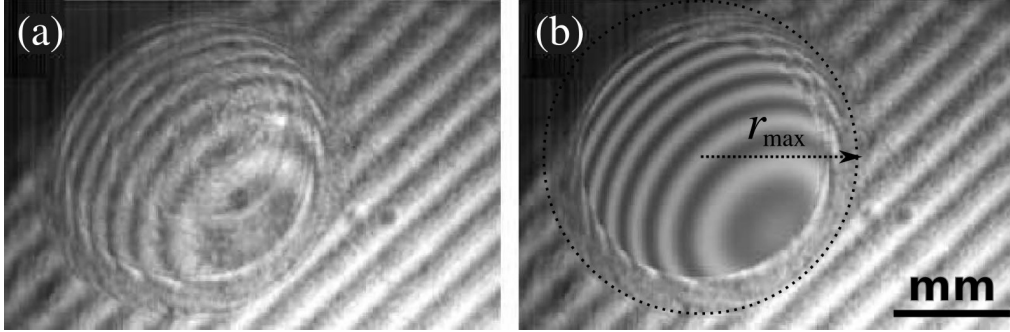
Fig. 3.1 (**a**) Interference pattern of a relaxed ^{3}He crystal. (**b**) Simulated pattern of cylindrical ECS [solution of equation (3.1)] inserted to it.

symmetric form given by the second-order differential equation,

$$\frac{1}{\lambda^2}(h - h_0) + \frac{r''_{hh}}{(1 + (r'_h)^2)^{(3/2)}} - \frac{1}{r(1 + (r'_h)^2)^{(1/2)}} = 0, \qquad (3.1)$$

where r is the radius of the crystal at a vertical position h of the interface.

This differential equation (3.1) can be solved numerically using trial capillary length λ and fixed boundary conditions. At the vertical crystal edge, $r'_h(0) = 0$, the diameter $2r_{max}$ of the crystal can be used to fix the boundary condition $r(0) = r_{max}$. At the top of the crystal the other boundary condition $h'_r(r = 0) = 0$ is satisfied which also uniquely determines the reference vertical position h_0.

For a trial λ the interference pattern corresponding to the cylindrical ECS was generated and compared with the original interferogram. Repeating this procedure with different λ, the range of capillary lengths λ which generate a matching interference pattern was found. Within the experimental error no remarkable temperature dependence was found for α. In addition, the obtained average capillary length $\lambda = 0.93 \pm 0.10$ mm, or, the surface tension $\alpha = 0.052 \pm 0.011$ mJ/m^2 agrees with the capillary length 1.03 ± 0.09 mm obtained between 140 mK and 330 mK by Rolley et al.[27]

From the result that the surface tension of the liquid-solid interface of ^{3}He does not significantly decrease when temperature decreases, one may conclude that the appearance of facets on ^{3}He crystals well below T_R is not related to the change in the value of the surface tension. Rather, facets appear below 100 mK on ^{3}He crystals due to the enhanced pinning of the liquid-solid interface to the crystal lattice.

3.2 Faceting of ^{3}He crystals

The roughening transition temperatures predicted by the universal relation (1.6) for the first three types of facets on ^{3}He crystals, (110), (100), and (211), are correspondingly at 260 mK, 130 mK, and 87 mK. Before the work described in this Thesis, the (110) facet has been seen at 100 mK [27], the (100) and (211) facets at 10 mK [52], and eight more facets at 0.55 mK [53,34]. The discrepancy between the predicted roughening temperature T_R and the highest temperature at which facets have been observed $T_{R,\mathrm{obs}}$ seemed to be relatively even larger for the (100) and (211) facets. In this Thesis work, the appearance of other than the basic (110) facet has been studied in Paper **II** with ^{3}He crystals at temperatures between 8 and 55 mK, in order to find out whether the (100) and (211) facets and higher order facets with smaller d appear relatively at lower temperatures than predicted by the universal relation.

The appearance of facets was studied with growing ^{3}He crystals, since the step energies of facets are really small close to their roughening transitions and consequently, as seen from equation (1.15), the resulting equilibrium facet size is also very small. Therefore, close to their T_R large facets can be seen only during crystal growth. However, the growth should not be too fast, since at least two effects can destroy facets during fast growth. Firstly, if the growth velocity of a crystal exceeds the critical velocity of Mullins–Sekerka instability [54] in the solidification front, then there appear "fingers" which soon will develop into dendrites similar to snowflakes. The critical velocity is size-dependent and for ^{3}He crystal at 50 mK with diameter of 1 mm it equals 0.2 µm/s. Secondly, the Pomeranchuk effect lowers the temperature of the growing crystal surface and if the pressure difference Δp, which develops between the melting pressure of the crystal surface at a lower temperature and the melting pressure for the liquid far from the crystal at a higher temperature, exceeds the nucleation threshold of $\delta p \sim 0.3$ kPa, a new crystal nucleates and grows instead of the existing one. The critical crystal growth velocity for such a nucleation is $(\delta T \, \kappa)/(LD) \sim 0.1$ µm/s at 50 mK, where $\delta T = (\mathrm{d}T/\mathrm{d}p)_{\mathrm{MC}}\delta p$, $(\mathrm{d}T/\mathrm{d}p)_{\mathrm{MC}}$ is the slope of the melting curve, κ is the thermal conductivity of liquid, L is the latent heat per unit crystal volume, and D is the cell size.

In Paper **II** it is demonstrated how to grow ^{3}He crystals covered with higher order facets which are relatively closer to their T_R than the (110) facet. ^{3}He crystals were found to show facets for which the angle between the
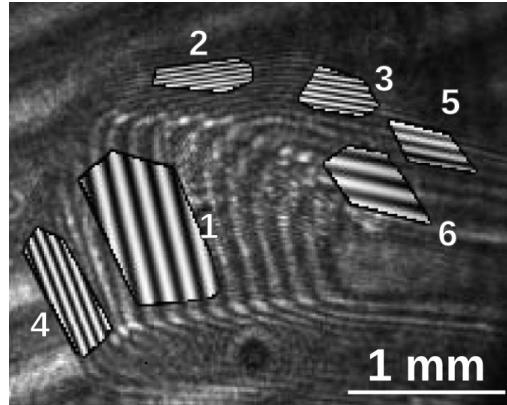
Fig. 3.2   Interferogram of a growing ^{3}He crystal at 55 mK—facets 1–6 are shown with fitted intensity distributions.

normal vectors of the adjacent facets is much smaller than 45°, which is the smallest angle which the two basic facets types, (110) and (100), can form. In Figure 3.2 is shown such a single ^{3}He crystal at 55 mK. The angle between facets 3 and 6 is 30° ± 5° and, as the facet 5 is between facets 3 and 6, the angle between facets 3 and 5, or, between facets 5 and 6 is even less. Due to the presence of high order facets, the crystal orientation could not be unambiguously determined and the presence of small angles thus suggests that at least 3 different types of facets should exist on ^{3}He crystals up to 55 mK, which is in line with the universal relation (1.6).

3.3   Roughening of ^{3}He crystals

The critical theory of roughening developed by Nozières and Gallet[28] has been used to explain the temperature dependence of the step energy of the basal c-facet on ^{4}He crystals close to the roughening temperature $T_R = 1.30$ K[55]. However, on ^{3}He crystals the temperature dependence of the step energy of the basal (110) facet which appear below 0.1 K, well below the roughening temperature $T_R = 0.26$ K, cannot be explained by the same theory.

The absence of facets on ^{3}He crystals well below T_R has been explained by Rolley *et al.*[27] who proposed that the quantum fluctuations of the interface reduce the step energy and broaden the roughening transition. If an

overpressure is applied on a finite-size crystal, which exceeds the threshold overpressure of 2D nucleation, the crystal roughens dynamically and the blurred transition takes place below T_R[28]. The proposed dynamic roughening explains the weak coupling ($\frac{\beta_{110}/d}{\alpha} \approx 0.01$) of the (110) facet to the lattice near 100 mK, where the step energy β_{110} of the (110) facet is smaller than 0.2 fJ/m[27], but this coupling has been found to be nearly strong ($\frac{\beta_{110}/d}{\alpha} \approx 0.4$) at 0.55 mK, where β_{110} is 6.6 fJ/m[34].

In order to find out the temperature dependence of the step energy, in this Thesis the growth dynamics of the (110) facets on ^{3}He crystals has been studied in Papers **III** and **IV** in a wider temperature range from 60 mK to 100 mK. In Figure 3.3 is shown the growing ^{3}He crystal near the temperature where facets appear. The growth of the facets was interpreted to be due to the spiral motion of steps through screw dislocations, thus the step energy could be obtained by measuring the quadratic dependence of the facet velocity v on the overpressure δp that drives the facet growth.

The small, of the order of 1 Pa overpressures were determined using the crystal surface as a sensitive (~ 0.1 Pa) overpressure gauge. In this method the overpressure on the facet δp_F is obtained with respect to the overpressure
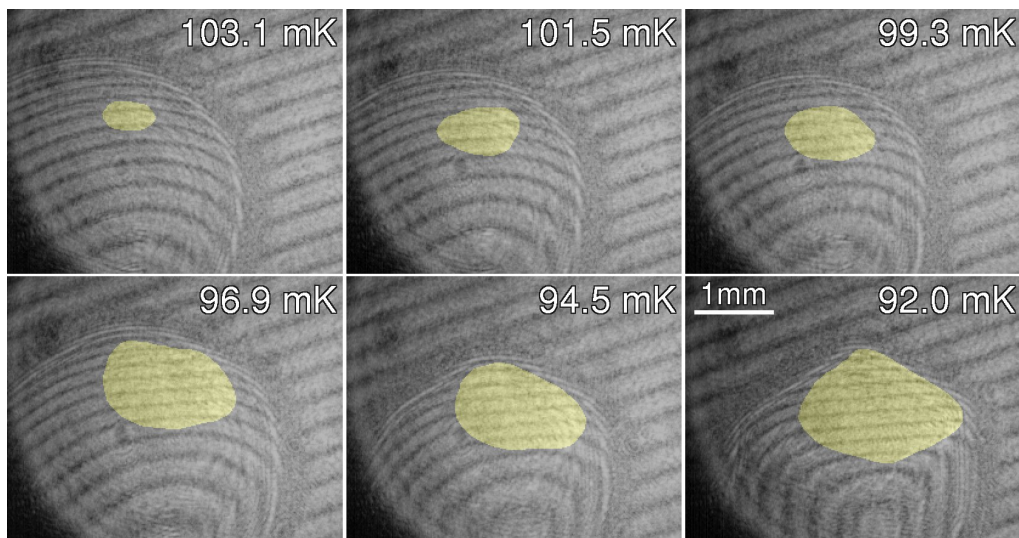

Fig. 3.3 Interferograms of a growing ^{3}He crystal near 100 mK. On the top of the growing crystal the size of the basic (110) facet (*highlighted area*) increases with respect to the diameter of the crystal when temperature decreases below 100 mK. The areas have been colored using Chirp z-transform (see section 2.2.3).

on the rough surface given in equation (1.4) which is used as a reference,

$$\delta p_F - \delta p_R = -\rho_l g(h_F - h_R) + \frac{\rho_l}{\Delta \rho_{sl}} \alpha \kappa_R \qquad (3.2)$$

The differential growth coefficient of the rough surface was calculated assuming that all the latent heat of crystallization is released in the liquid side[43,44], so that the sharing coefficient of the latent heat L is $\lambda = TS_s$. In the studied temperature range solid ^{3}He conducts heat much better than liquid ^{3}He, $Z_s \ll Z_l$, and if the characteristic scale of velocity variation is larger than $R_K \kappa_l \approx 10\,\mu$m, then $R_K \ll Z_l$. The isothermal growth coefficient k is large and can be omitted far away from the melting curve minimum temperature $T_{\mathrm{MCM}} = 315\,$mK. Thus the equation (1.23) of the rough surface mobility reduces into equation (1.25) which can be written in terms of overpressure as

$$\left(\frac{d\delta p}{dv}\right) = \mu_R^{-1} = \frac{\rho_s \rho_l}{\Delta \rho_{sl}} k_{\mathrm{eff}}^{-1} = \frac{\rho_s^2 \rho_l R_K L^2}{\Delta \rho_{sl} T}. \qquad (3.3)$$

Here $L = T(S_s - S_l)$ is the latent heat. In the temperature range from $0.05\,$K to $0.25\,$K the value of the Kapitza resistance R_K varies inversely proportionally to T^3 according to the acoustic mismatch theory,

$$R_K T^3 = 3.3 \cdot 10^{-6}\,\mathrm{m^2 K^4/W}, \qquad (3.4)$$

as measured by Amrit and Bossy[56] who also suggested $\lambda = TS_s$. In Paper **IV** the measurements on the growth dynamics of the rough surface have confirmed relation (3.3) with 10% accuracy in the temperature range from $0.06\,$K to $0.10\,$K.

The growth of the faceted surface is not uniform, as it is in the case of the rough surface. On one hand, on the rough surface atoms stick uniformly and, on the other hand, on facets atoms stick non-uniformly but only at the steps. Each sticking event is associated with the elaboration of latent heat L. Due to the different distribution of sticking events on the rough surface and on the faceted surface, there appear several scales for the latent heat diffusion. At the rough surface latent heat is elaborated uniformly, but on the steps latent heat is elaborated at the steps, and no latent heat is elaborated between steps, where there are no sticking events, thus the temperature jump across the interface is there the smallest.

The temperature jump across the facet can be found for the steps far from the screw dislocation which move at velocity v_{st} and have an asymptotic

distance l. Such a periodical distribution of moving steps can be described by a sum of velocity harmonics, $v(x) = \sum_{q=2\pi/l}^{2\pi/\xi} v_q \cos(qx)$. Linear heat diffusion equation can be analytically solved for each velocity harmonic. The sum over q then yields the total heat distribution over the facet. For steps which move at a velocity which is much slower than the diffusion of heat between the steps, $v_{st} \ll \kappa_l q/C_l$, where C_l is the specific heat of the liquid, the delay in the moving temperature profile for the set of steps can be neglected. Then thermal distribution over the facet is static and, as it is found in Paper **IV**, the equation for the step motion is

$$v_{st} = \frac{\pi\kappa_L T \rho_{sl}}{L^2 \rho_s^2 \rho_l d \ln l/\xi} \left[\delta p_F - \delta p_R + \frac{\rho_s^2 \rho_l R_K L^2}{\Delta\rho_{sl}T}(v_R - \langle v_F \rangle) \right]. \qquad (3.5)$$

Here the term in square brackets is the effective overpressure δp_{eff} that drives step motion and the term before it is the step mobility μ_{st}. Since the logarithm $\ln l/\xi$ varies very slowly with the distance between steps l, one can use the equation for the asymptotic distance between the neighboring steps[57],

$$l \approx 20\beta\rho_l/(d\Delta\rho_{sl}\delta p_{\mathrm{eff}}),$$

and obtain the well-known quadratic dependence of the facet velocity v_F on the effective overpressure δp_{eff},

$$v_F = (d/l)v_{st} = \frac{\pi\, d\,\kappa\,T}{20\beta L^2 \ln(l/\xi)} \left(\frac{\Delta\rho_{sl}}{\rho_s\rho_l} \right)^2 \delta p_{\mathrm{eff}}^2. \qquad (3.6)$$

The quadratic dependence of v_F to p_{eff}, which was used to find out the step energy β, is shown in the insert of Fig. 3.4. Due to the step mobility μ_{st} which strongly depends on temperature, the facet velocities at 64 mK can be estimated to be only about twice larger than at 0.55 mK.

The measured temperature dependence of β shown in Fig. 3.4 reveals that the interface-to-lattice coupling is weak in ^{3}He in the temperature range of 50–100 mK. Equation (1.10) which describes the renormalization of the step energy β by thermal fluctuations can be well fitted to the β vs. T data measured in the temperature range of 50–100 mK. By setting the short scale cut-off to $k_0 = \sqrt{2/3}\pi/d$ which is the value for the highest possible wave vector of the (110) plane, the obtained value for the pinning potential V_0 is by three orders of magnitude smaller than the value of the surface stiffness α, which makes it impossible to explain the nearly strong coupling $(V_0/\alpha \sim 1)$ at 0.5 mK[34]. Therefore a new theory which incorporates quantum fluctuations is needed to explain the full temperature dependence of β.
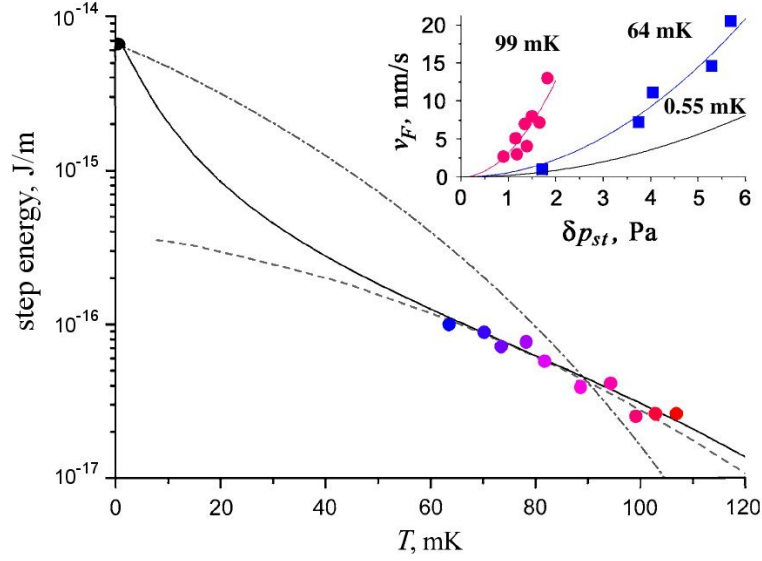
Fig. 3.4 The step energy of the (110) facet on ^{3}He crystals as a function of temperature. The *filled circle* at 0.55 mK is from Ref.[34] **Insert:** The quadratic dependence of the facet velocity v_F to the overpressure δp. The *lowest curve* extrapolates the δp vs. v_F data at 0.55 mK[34] quadratically to low pressures.

To incorporate the quantum fluctuations the dynamic version of the renormalization group theory can be used. When using the Langevin equation (1.12) the renormalization proceeds in the same manner both in the cases of thermal and quantum distribution of fluctuations. The only difference is in the correlation coefficient of the random force R which must be written in a general form which is valid both in quantum and classical cases[58],

$$R_{k,\omega}^2 = \eta\hbar\omega \coth(\hbar\omega/2k_BT). \tag{1.14}$$

In the zero limit of the Planck constant, $\hbar \to 0$, equation (1.14) reduces to the classical white noise spectrum given in equation (1.13). Due to quantum fluctuations, the amplitude of fluctuations $\langle z^2 \rangle$ changes to

$$\langle z^2 \rangle = \frac{\hbar}{4\pi^2\gamma} \int_0^{\omega_0} d\omega \coth\frac{\hbar\omega}{2T}\Big(\text{atan}\frac{\gamma k_0^2}{\omega\eta} - \text{atan}\frac{\gamma k_*^2}{\omega\eta}\Big). \tag{3.7}$$

As suggested by Puech *et al.*, the intrinsic damping coefficient η varies as $1/T$. For a reference, the value measured at the melting curve minimum temperature, $\eta(315\,\text{mK}) = 660\,\text{kg}/(\text{m}^2\text{s})$[43], is used.

All the experimental data on the step energy at different T can be fitted with equations (1.10), (1.8) and (3.7), with only two fitting parameters, k_0

and ω_0. The fitted value of the short-scale cut-off $k_0 = 1.9/d$ is close to the value for the highest possible wave vector of the (110) plane $\sqrt{2/3}\pi/d$, and the value for the high frequency cut-off $\omega_0 = 7.4 \cdot 10^{11}$ 1/s agrees well with the frequency range measured in the inelastic neutron scattering[59].

One may conclude that the coupling of the liquid-solid interface of ^{3}He to the crystal lattice is extremely weak below the roughening temperature at 0.26 K down to 0.1 K due to the quantum fluctuations of the interface which significantly reduce the step energy. Below 0.1 K quantum fluctuations become more and more damped due to the Fermi-degeneracy of the liquid which creates a bottle-neck for the spin transport through the moving interface, which allows the facets to show up. At ultra low temperatures the quantum fluctuations are strongly damped, the coupling is nearly strong and the interface is well-localized as it is in classical crystals.

Due to the strong damping of the surface fluctuations, the interface-to-lattice coupling at ultra-low temperatures is in ^{3}He even stronger than in ^{4}He, which one would not expect on the base of the zero-point oscillations of atoms which are larger for ^{3}He atoms than for ^{4}He atoms. Apparently quantum fluctuations reduce also the step energy in ^{4}He, but the reduction of the step energy is much smaller in ^{4}He because the surface tension in ^{4}He is nearly three times larger than in ^{3}He. The reduction of the step energy due to quantum fluctuations in ^{4}He does not depend on temperature because the surface oscillations (crystallization waves) are weakly damped and their spectrum is temperature-independent[5].

3.4 Critical size of facets on the surface of ^{3}He crystals at temperatures close to T_N

Tsepelin *et al.*[34] have found that the interface-to-lattice coupling in ^{3}He crystals is nearly strong at the lowest temperatures, where the solid ^{3}He has the antiferromagnetic u2d2 ordering. The step energies of facets on ^{3}He crystals 0.55 mK have, however, been measured only at a single temperature and by analyzing the data on growing facets, which required several assumptions. In order to confirm the results by Tsepelin *et al.* on the steps energies and to find out the step energies in a wider temperature range, the (110) and (100) facets have been studied in Paper **V** in a quasi-static situation during slow melting of the crystal.
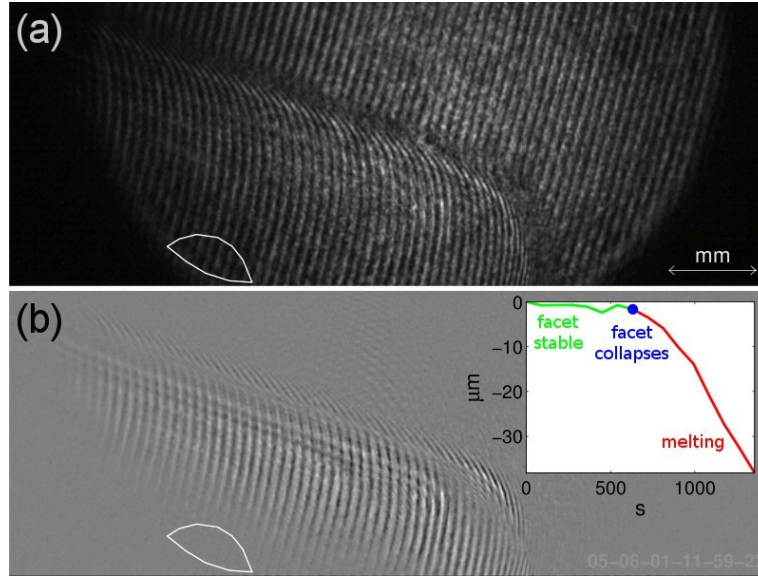
Fig. 3.5 A slowly melting ^{3}He crystal at $1.1\,\mathrm{mK}$. (**a**) Original interferogram. The horizontal (100) facet is bordered with the white line. (**b**) Image showing the difference between the intensities of the interferograms at the beginning of the melting series and just before the facet collapsed. In the area where the (110) facet has been immobile, the phase difference, and, the intensity difference vanishes. **Insert:** Development of the vertical position of the (100) facet.

The melting of faceted ^{3}He crystals was carried out both below and above the magnetic ordering transition temperature of solid ^{3}He at $T_N = 0.902\,\mathrm{mK}$. During slow melting of the crystal, facets first remain immobile and only their sizes decrease. When the critical radius R_c of a facet is reached, the facet collapses, as is shown in Fig. 3.5. The step energies of facets were determined using equation (1.16) by measuring R_c and the corresponding overpressure on the facet δp_F.

Before the facet collapsed, the size of the facet decreased relatively slowly compared to the time of taking the interferograms, therefore the critical size of the facet was determined from the interferogram at the moment just before the facet was seen to collapse. The overpressure on the facet was determined by comparing the overpressure on the reference rough surface,

$$\delta p_F = \frac{\rho_l}{\Delta \rho_{sl}} \alpha \kappa_R - \rho_l g (h_F - h_R) + \frac{v_R}{\mu_R}. \tag{3.8}$$

The overpressure on the facet was thus determined from the shape of the crystals as seen in the interferograms, namely from the height h_F at a point

on the edge of the facet and from the height h_R and curvature κ_R at a point on the reference rough surface, and no special pressure measurement was needed. The mobility of the rough surface μ_R was used to find the reference overpressure $\delta p_R = v_R/\mu_R$.

The value of μ_R was determined from the dynamics of the rough surface by measuring the v_R vs. δp_R dependence using equation (1.4). At 1.1 mK, the value of $\mu_R = 0.044\,(\mu\text{m/s})/\text{Pa}$ was measured. The mobility of the rough surface, or, the growth coefficient measured in this way corresponds to the thermal impedance between different parts of the surface and can be therefore called as differential growth coefficient. In previous measurements[38,39,40,41] of the growth coefficient of the rough surface the values of k_R were smaller and were due to the thermal impedance of the liquid between the crystal surface and the sinter, including the sinter, and were not therefore applicable in using the crystal surface as an overpressure gauge.

The results obtained with the method of slow melting of facets are shown in Fig. 3.6. The step energy obtained for the (110) facet, $\beta_{110} = 4.7 \pm 0.3\,\text{fJ/m}$, and for the (100) facet, $\beta_{100} = 1.1 \pm 0.2\,\text{fJ/m}$, agree well with the values obtained by Tsepelin $et\ al.$ with the spirally growing crystals at 0.55 mK[34].

The kinetic correction, v_R/μ_R, to the overpressure δp_F results in the reduction of the value of step energy. Below T_N, the value measured for μ_R at 1.1 mK would result in the reduction of 5–20% of the step energies, but above T_N the reduction of the step energy due to the kinetic correction would be up to 10 times larger than the measured value of the step energy. Since the step energy can be only non-negative, the values measured for the mobility of rough surface are far too low.

Another way to estimate the mobility of rough surface from below is to utilize the facet growth measurements at 0.55 mK[34]. In those measurements the facet velocity depended linearly on the applied overpressure, as described in equation (1.19), already at as low overpressures as 5 Pa, which means that the step moved at the critical velocity $v_c = 7\,\text{cm/s}$. The mobility of the step obtained from this observation is $\mu_{\text{st}} \gtrsim 1\,(\text{cm/s})/\text{Pa}$. Considering the step as a rough surface and taking into account the width of the step given in equation (1.17), $(\xi/d) = \frac{2}{\pi^2}\alpha/(\beta/d) \approx 1$, the mobility of the rough surface[28] at 0.55 mK is $\mu_R = \frac{2}{\pi^2}(d/\xi)\mu_{\text{st}} \gtrsim 0.2\,(\text{cm/s})/\text{Pa}$. The value of $\mu_R^{-1} = \frac{\rho_l\rho_s}{\Delta\rho_{sl}}k_{\text{eff}}^{-1}$ can be scaled within the studied range of temperatures using the L^2/T dependence presented in relation (1.24), as the latent heat
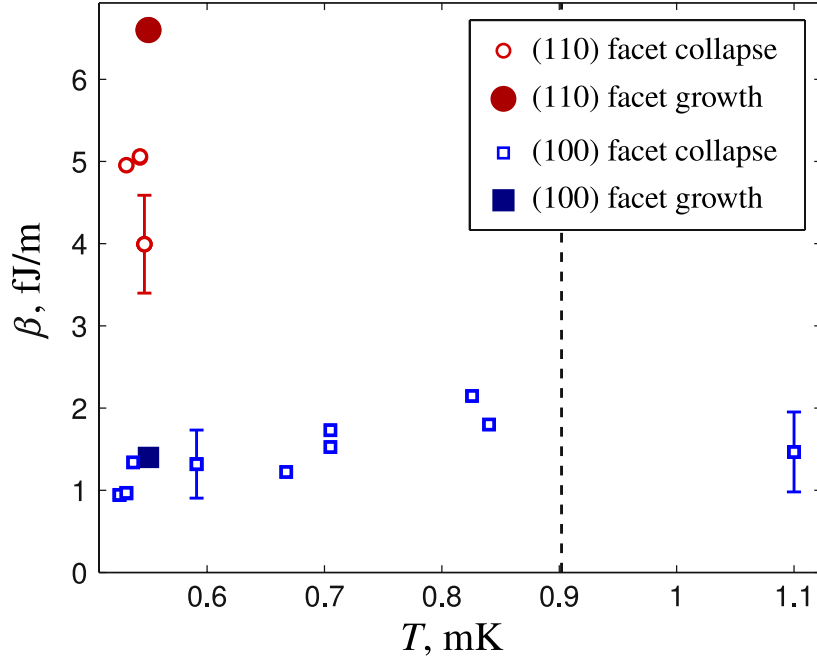
Fig. 3.6 Step energies measured with the collapsing (110) facets (*open circles*) and (100) facets (*open squares*); for discussion on the kinetic correction, see text. The results agree with the earlier measurements on spirally growing facets (*filled symbols*) by Tsepelin *et al.*[34]

transport limits the growth of the rough surface[5] and the temperature dependence of the thermal impedance of liquid is negligible below $0.7T_c$[60,61]. This kind of estimation yields that below T_N the kinetic correction would be negligible and above T_N the value of $\mu_R(1.1\,\mathrm{mK}) \gtrsim 4\,(\mu\mathrm{m/s})/\mathrm{Pa}$ would result in only 10% reduction of the step energy, being thus within the experimental accuracy of the step energies without kinetic correction.

In the measurements presented in Paper **V** the critical radius of facets was measured on helium crystals for the first time. The obtained step energies agree with the earlier measurements by Tsepelin *et al.*[34], thus at the lowest temperatures the interface-to-lattice coupling in ^{3}He crystals, $\frac{\beta_{(100)}/d}{\alpha} = 0.25$, indeed is stronger than in ^{4}He crystals, $\frac{\beta_{(0001)}/d}{\alpha} = 0.07$ [28,62]. The step energy of the (100) facet was found to be roughly constant below T_N and did not show increase above T_N. As predicted in Paper **III**, the observed step energies were found not to be significantly affected by the antiferromagnetic transition of solid ^{3}He. Although the antiferromagnetic ordering of nuclear spins in solid ^{3}He was not found to significantly affect
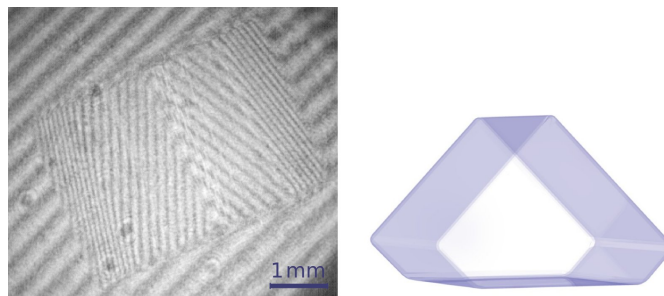
Fig. 3.7 A growing bcc ^{3}He crystal at 1.07 mK: (left) interference pattern and (right) 3D reconstruction from front. In the vicinity of the spin-ordering transition of solid ^{3}He at 0.902 mK (see Fig. 1.3), the (100) facets grow much slower than the (110) facets and, as a result, the crystal have taken the form of a cube.

the energy of an elementary step on the facet, the growth dynamics of ^{3}He crystals could be strongly affected by the spin currents, which can be seen in Fig. 3.7.

3.5 Remark on the growth of ^{4}He crystals near the first roughening transition

The roughening of ^{4}He crystals has been thought to be well understood within the frame of the renormalization group theory[37]. Indeed, the step energy of the basal (0001) facet measured below the roughening temperature $T_R = 1.3$ K down to 1.130 K has been observed to renormalize with the thermal fluctuations[63,29].

In those measurements the chemical potential difference that drives the crystal growth, $\Delta\mu = \Delta\rho_{sl}gH/\rho_s$, was measured from the height difference H between the crystal under study and the reference crystal which had a large horizontal surface. The growth velocities of the (0001) facet were found to vary exponentially which suggests the 2D nucleation process to dominate[63,29],

$$v_F \propto \Delta\mu \exp\left(\frac{-\pi\beta^2}{3d\Delta\mu k_B T}\right), \qquad (3.9)$$

so that $\ln(v_F/\Delta\mu)$ was linear to $1/\Delta\mu$. The slope of the linear dependence resulted in the value of β.

In the work described in this Thesis, the possibility of the growth of ^{4}He crystals near T_R through screw dislocations has been reconsidered in Paper **VI**. In the spiral growth of steps the velocity of facets varies as

$$v_F = \frac{K\rho_s d^2 k_{\mathrm{st}}}{19\beta}\Delta\mu^2, \tag{3.10}$$

where k_{st} is the growth coefficient of the step. In the original analysis the growth of the step has been considered as growth of a rough surface, $k_{\mathrm{st}} = k_R$. With this assumption the spiral growth would have given much smaller growth velocity than in the case of 2D nucleation for the same driving force $\Delta\mu$.

However, the theory of critical fluctuation by Nozières and Gallet[28], which was used to interpret the temperature dependence of the step energy, predicts also that near T_R the step is not sharp. Instead, the step has a finite width ξ which is inversely proportional to β, according to equation (1.17). The step can be thought as an interface tilted by a small angle $\sim d/\xi$, in which case the growth coefficient of the broadened step will be

$$k_{\mathrm{st}} = \frac{\pi^2}{2}(\xi/d)k_R = \frac{\gamma d}{\beta}k_R. \tag{3.11}$$

For the surface stiffness of $\gamma \approx 0.24\,\mathrm{mJ/m^2}$ [63] and the step energy of $\beta(1.130\,\mathrm{K}) = 0.11\,\mathrm{fJ/m}$, the step width would be even $\sim 600d$. The growth coefficient of the step k_{st} would accordingly be 600 times larger than the growth coefficient of the rough surface. If the temperature of the facet is closer to T_R, the value of β is smaller and this factor would be even larger. Combining equations (3.10) and (3.11) leads to the facet velocity

$$v_F = \frac{K\gamma d^3 k_R}{19\beta^2}\Delta\mu^2, \tag{3.12}$$

where $K = 2$ for the c-facet and $k_R/\rho_s = 3.1 \cdot 10^{-4} \exp(7.8\,\mathrm{K}/T)\,\mathrm{s/m}$ [63,28].

With the assumption that 2D nucleation is more effective than spiral growth, the step energies $\beta(1.130\,\mathrm{K}) = 0.14\,\mathrm{fJ/m}$ and $\beta(1.173\,\mathrm{K}) = 0.063\,\mathrm{fJ/m}$ [63], and $\beta(1.205\,\mathrm{K}) = 0.0084\,\mathrm{fJ/m}$ [28] have been obtained. The measured average distance between the screw dislocations $\langle l \rangle \approx 0.1\,\mathrm{mm}$ [63] results in the growth thresholds of Frank-Read sources $\Delta\mu_{\mathrm{thr}} = \beta/[d\rho_s(\langle l \rangle/2)]$, which at the temperatures mentioned before are $\Delta\mu_{\mathrm{thr}}(1.130\,\mathrm{K}) = 0.5\,\mathrm{cm^2/s^2}$, $\Delta\mu_{\mathrm{thr}}(1.173\,\mathrm{K}) = 0.2\,\mathrm{cm^2/s^2}$, and $\Delta\mu_{\mathrm{thr}}(1.205\,\mathrm{K}) = 0.03\,\mathrm{cm^2/s^2}$. These growth thresholds are by more than an order of magnitude smaller than the
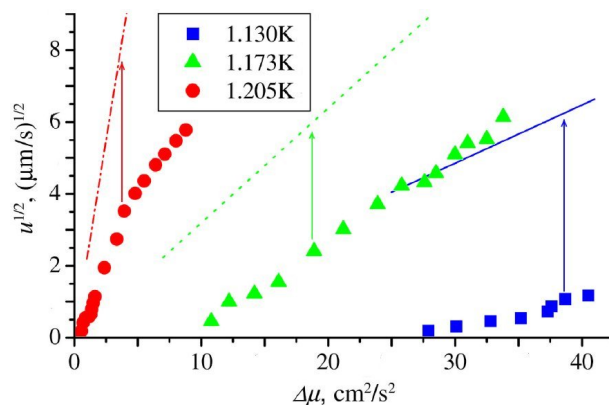
Fig. 3.8 Velocities vs. driving forces of the (0001) facet, as measured by Wolf *et al.*[63] (1.130 K and 1.173 K) and by Gallet *et al.*[29] (1.205 K). The spiral growth (*lines*) would give larger growth velocities at the same driving forces with the reported step energies.

actual driving forces measured in the experiment. Thus the actual driving forces are large enough to provide spiral growth. If the growth velocities due to the 2D nucleation and due to the spiral growth are being compared with the step energies found by assuming 2D nucleation, it is found that the growth velocities of the facet through spiral growth would be more effective than via 2D nucleation at all temperatures and at all measured driving forces, as it is illustrated in Fig. 3.8.

To conclude, the theory of critical fluctuations[28] which has been used to explain the roughening of the (0001) facet on ^{4}He crystals gives also a prediction for the step width given in equation (1.17). If the prediction on the step width is correct and it indeed diverges when approaching T_R then, as it is found in Paper **VI**, spiral growth should have been more effective than 2D nucleation in the studies by Wolf *et al.*[63] and Gallet *et al.*[28]. In order to obtain adequate understanding on the roughening of ^{4}He crystals, the role of spiral growth should therefore be reconsidered either in these measurements or in a new series of measurements.

Chapter 4

Studies on the liquid-solid interface of ^{4}He

4.1   High-accuracy measurements of the melting pressure

The study of "supersolidity" has leaded to various experiments in which mainly the dynamic properties of the solid has been investigated. In the work described in this Thesis the equilibrium properties of solid ^{4}He have been studied in Papers **VII**, **VIII**, and **IX** with the most convenient way, by measuring the melting pressure of ^{4}He. If the transition to "supersolid" state is a real phase transition, the entropy should show an anomaly at the transition, which might show up at the melting curve of ^{4}He. Although there exists results of earlier measurements on the melting curve of ^{4}He[64,36], the accuracy of these measurements was not good in the temperature range where the possible superfluid phase has been proposed to exist.

According to the Clausius–Clapeyron equation the slope of the melting curve is proportional to the entropy difference between liquid and solid,

$$\left(\frac{dP}{dT}\right)_{\mathrm{MC}} = \frac{S_l - S_s}{\nu_l - \nu_s} = \frac{L}{T\Delta\nu_{ls}},\tag{4.1}$$

where ν_l and ν_s are the molar volumes of liquid and solid. The entropy of hcp solid ^{4}He below $0.5\,\mathrm{K}$ is due to phonons, with the effective Debye

temperature $\Theta \approx 26\,\mathrm{K}$, which leads to the heat capacity of solid ^{4}He

$$C_V^s = \frac{12}{5}\pi^4 R \left(\frac{T}{\Theta}\right)^3, \tag{4.2}$$

where R is the gas constant. The entropy of superfluid ^{4}He below $0.5\,\mathrm{K}$ is also due to phonons, moving at sound velocity $c = 366\,\mathrm{m/s}$, which yields the heat capacity of liquid ^{4}He

$$C_V^l = \frac{2}{15}\pi^2 \frac{R}{n_l} \left(\frac{k_B T}{\hbar c}\right)^3, \tag{4.3}$$

where n_l is density of atoms in liquid. The specific heat, $C_V \equiv T\left(\frac{\partial S}{\partial T}\right)_{N,V}$, of both solid C_V^s and liquid C_V^l is proportional to T^3, therefore also the slope of the melting pressure $\left(\frac{dP}{dT}\right)_{\mathrm{MC}}$ varies as T^3. Any thermodynamical transition would thus be seen as a deviation from the T^4 dependence of the melting pressure.

The melting curve of pure ^{4}He ($80\,\mathrm{ppb}$ of ^{3}He) measured in Paper **VII** shows that the T^4 law is obeyed below $0.4\,\mathrm{K}$ down to $80\,\mathrm{mK}$ within the experimental accuracy of $\pm 0.05\,\mathrm{Pa}$. The variation of the melting curve, $-3.42 \pm 0.02\,\mathrm{kPa/K^4}$, agrees well with the earlier measurements on the sound velocity and density of liquid and entropy of solid ^{4}He[65] from which the variation of $-3.6\,\mathrm{kPa/K^4}$ can be found, and on the heat capacity measurements on solid ^{4}He[66] from which the variation of $-3.47\,\mathrm{kPa/K^4}$ can be found. Below 80 mK the melting curve, which is shown with the solid line in Fig. 4.1, seemed to increase by about $0.5\,\mathrm{Pa}$ over the T^4 behavior.

In our later results published in Paper **VIII** this increase was attributed to the temperature dependence of the pressure gauge sensitivity. The beryllium bronze, which was used as the material for the flexible membrane of the capacitive pressure, is known to have high tensile strength and low losses on mechanical deformation but some types of beryllium bronze are also known to have a low temperature anomaly in heat capacity[67] and in Young modulus[68]. The increase of $\sim 0.5\,\mathrm{Pa}$ at $2.5\,\mathrm{MPa}$ absolute pressure corresponds to the change of $0.5\,\mathrm{Pa}/2.5\,\mathrm{MPa} = 2 \cdot 10^{-7}$ in sensitivity of the pressure gauge below $80\,\mathrm{mK}$.

The sensitivity of the pressure gauge have been taken into account in the later measurements in Paper **VIII** on the melting pressure of ultra-pure ^{4}He ($0.3\,\mathrm{ppb}$ of ^{3}He). As can be seen in Fig. 4.1, the melting pressure measured with the pure and ultra-pure ^{4}He do not significantly differ—in
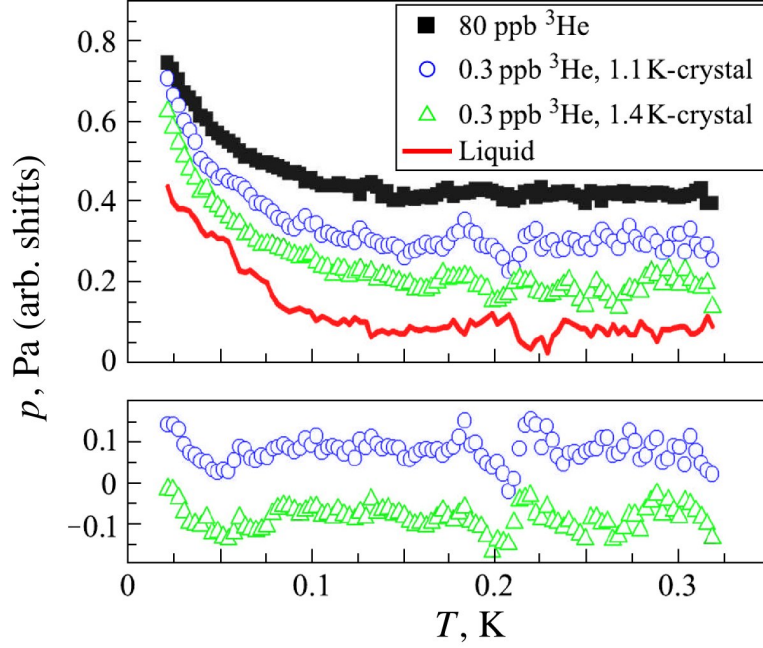
Fig. 4.1 *Upper:* The measurements on the melting pressure of pure ^{4}He (80 ppb of ^{3}He) [**IV**] and ultra-pure ^{4}He (0.3 ppb of ^{3}He) [**VII**] and on the pressure of liquid ^{4}He in constant volume at 2.51 MPa [**VII**]. *Lower:* The deviation of the melting pressure from the T^4 dependence is within ~ 0.05 Pa after the correction (see text).

both measurements the low temperature tail is present. With the ultrapure ^{4}He the heat expansion of the liquid ^{4}He at a constant volume was also measured. The liquid ^{4}He was first pressurized close to the melting pressure and the constant volume was provided by the cold valve attached to the mixing chamber.

The thermal expansion of the liquid helium at a constant volume varies as

$$\left(\frac{\partial p_l}{\partial T}\right)_V = -\frac{\rho}{V}\left(\frac{\partial S}{\partial \rho}\right)_T. \qquad (4.4)$$

As the heat capacity of liquid $[C_V \equiv T\left(\frac{\partial S}{\partial T}\right)$ is given in equation (4.3)] is due to phonons, the entropy varies as $S \propto T^3(\frac{V}{c^3})$. Noting in addition that $\frac{\partial}{\partial \rho}(\frac{V}{c^3}) = V(\frac{\partial c}{\partial \rho})\frac{\partial}{\partial c}(\frac{1}{c^3}) + \frac{1}{c^3}\frac{\partial}{\partial \rho}(V)$ and $V = \frac{M_l}{\rho}$, where M_l is the molar mass of liquid, one obtains that the thermal expansion of the liquid at a constant

volume varies as

$$\left(\frac{\partial p_l}{\partial T}\right)_V = (3\,U_0 + 1)\frac{S}{V},\qquad(4.5)$$

where $U_0 = \frac{\rho}{c}(\frac{\partial c}{\partial \rho})$ is the Grüneisen constant. Consequently, the variation of liquid pressure, $p_l(T) - p_l(0\,\mathrm{K})$, is proportional to T^4.

In the measurements of the pressure of liquid helium described in Paper **VIII**, the deviation from the T^4 dependence was similar to that in measurement on the melting pressure. Indeed, when the T^4 dependence is subtracted from the pressure of the liquid at a constant volume (see solid line in Fig. 4.1), the same low temperature behavior is present both in the measurements of the melting pressure and of the pressure of liquid. When comparing the difference of the melting pressure and the heat expansion of liquid measurements, one may conclude that within about $0.05\,\mathrm{Pa}$ the low temperature anomaly is the same and is therefore attributed to the properties of the pressure gauge. Thus the melting pressure follows the T^4 dependence down to the lowest measured temperatures of $10\,\mathrm{mK}$ without any sign of a supersolid transition.

The upper limit for the excess entropy S_{exc} due to the supersolid fraction $(\rho_{\mathrm{ss}}/\rho_s)$ can be estimated from the experimental accuracy of the melting curve measurement, $\Delta(\frac{dP}{dT})_{\mathrm{MC}} \approx 0.05\,\mathrm{Pa}/0.3\,\mathrm{K}$. Differentiating the Clausius-Clapeyron equation (4.1) with respect to $(S_l - S_s)$ the upper estimate for the excess entropy is $S_{\mathrm{exc}} = \Delta(S_l - S_s) = \Delta(\frac{dP}{dT})_{\mathrm{MC}}(\nu_l - \nu_s) \approx 5 \cdot 10^{-8}R$, where R is the gas constant. The possible supersolid fraction $(\rho_{\mathrm{ss}}/\rho_s) \sim S_{\mathrm{exc}}/R \lesssim 5 \cdot 10^{-8}$ is thus by two orders of magnitude smaller than the earlier estimate of $5 \cdot 10^{-6}$ [8].

4.2   Elementary excitations in liquid and solid ^{4}He

In the work described in this Thesis the pressure of liquid ^{4}He at a constant volume was originally studied in Paper **VIII** in order to calibrate the sensitivity of the beryllium copper pressure gauge at temperatures below $0.1\,\mathrm{K}$. The heat expansion of liquid ^{4}He has been examined in detail in Paper **IX** to analyze the melting curve with well established thermodynamical properties of the liquid. Although there exists results of previous measurements [69,70]

on the heat expansion of liquid ^{4}He, the accuracy of these measurements is much less than what is needed to compare with our melting curve data.

The temperature dependence of the pressure $p_l(T) - p_l(0\,\mathrm{K})$ of liquid ^{4}He below $0.3\,\mathrm{K}$ at constant volume is well described by the T^4 dependence due to phonons,

$$p_{l,\mathrm{ph}} = (3U_0 + 1)\frac{\pi^2}{90}\frac{k_B^4}{\hbar^3 c^3} \cdot T^4 = 0.50\,\mathrm{kPa/K^4} \cdot T^4, \qquad (4.6)$$

where $U_0 = 2.21$ and $c = 366\,\mathrm{m/s}$[71]. Above $0.3\,\mathrm{K}$ there appears an additional contribution $p_{l,\mathrm{rot}}$ to to the liquid pressure due to rotons. From $p_{l,\mathrm{rot}}$ it is possible to find out the value for the roton gap Δ using the equation found in Paper **IX**,[1]

$$p_{l,\mathrm{rot}} = \left[\frac{\partial F}{\partial V_l}\frac{\Delta}{k_B} - F\frac{\partial \Delta}{k_B \partial V_l}\left(\frac{1}{2} + \frac{\Delta}{k_B T}\right)\right]\left(\frac{\Delta}{k_B T}\right)^{-3/2}\exp\left(-\frac{\Delta}{k_B T}\right),$$
$$(4.7)$$

where the values for factors $F = 2V_l k_B m_0^{1/2} p_0^2 \Delta^{1/2}/(2\pi\hbar^2)^{3/2}$, and for derivatives $\frac{\partial F}{\partial V_l}$ and $\frac{\partial \Delta}{\partial V_l}$ at $p_l = 2.51\,\mathrm{MPa}$ are taken from the measurements by Greywall[72,73].

The measurements on the variation of the liquid pressure $p_l(T) - p_l(0\,\mathrm{K})$ at constant volume are shown in Fig. 4.2, where the phonon contribution $p_{l,\mathrm{ph}}$ given in equation (4.6) has been subtracted. The solid line in Fig. 4.2 shows the contribution $p_{l,\mathrm{rot}}$ due to rotons with the value $\Delta = 6.95\,\mathrm{K}$ of the roton gap. This revised value is larger than the value $6.8\,\mathrm{K}$ reported in Paper **IX** and closer to the value $7.28\,\mathrm{K}$ given by Greywall measurements[72,73]. At $0.46\,\mathrm{K}$ the calculated $p_{l,\mathrm{ph}}$ deviates from the experimental points by almost $0.2\,\mathrm{Pa}$, which is small compared to the phonon contribution $p_{l,\mathrm{ph}}(0.46\,\mathrm{K}) = 27.3\,\mathrm{Pa}$ and may be due to the change of $0.25\,\mathrm{Pa/25\,MPa} = 10^{-8}$ in the sensitivity of our pressure gauge, as the Young modulus of beryllium copper is known to change not only below $0.1\,\mathrm{K}$ but also at higher temperatures[68].

In the melting curve of ^{4}He below $0.46\,\mathrm{K}$ the contributions from phonons and rotons are dominating as well. The melting curve data is shown in Fig. 4.3 with the fitted $p_{\mathrm{MC,ph}} = -3.61\,\mathrm{kPa/K^4} \cdot T^4$ term due to phonons both in liquid and solid subtracted.[2] The remaining temperature dependence of

---

[1]In Paper **IX** term $\frac{\Delta}{k_B}$ was missing from $p_{l,\mathrm{rot}}$ and should have been inserted after $\frac{\partial F}{\partial V}$.

[2]The $p_{\mathrm{MC,ph}}$ term here is from the melting curve data in Papers **VIII** and **IX**. The difference from $p_{\mathrm{MC,ph}} = -3.42\,\mathrm{kPa/K^4} \cdot T^4$ measured earlier in Paper **VII** can be attributed to the sensitivity of the ^{3}He melting curve thermometer and the sensitivity of the ^{4}He pressure gauge, which were calibrated more accurately in the latter experiments.
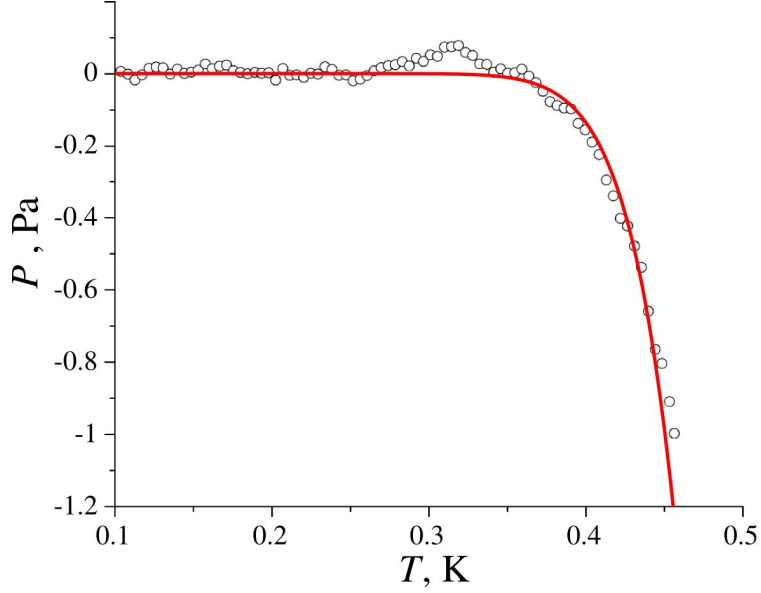
Fig. 4.2 Variation of the pressure $P_l(T) - P_l(0\,\mathrm{K})$ of liquid ^{4}He at constant volume after the T^4 term, found from the data below $0.32\,\mathrm{K}$, has been subtracted. *Solid line* is a fit of the roton contribution $p_{L,\mathrm{rot}}$ (see text).

p_{MC} can be attributed to the rotons,

$$p_{\mathrm{MC,rot}} = \frac{F}{\Delta V_{ls}} \frac{\Delta}{k_B} \left(\frac{\Delta}{k_B T} \right)^{-3/2} \exp\left(-\frac{\Delta}{k_B T} \right), \qquad (4.8)$$

with the revised gap value of $\Delta = 6.95\,\mathrm{K}$. The roton contribution $p_{\mathrm{MC},l}$ is shown in Fig. 4.3 with the solid line. There is also in the specific heat of solid ^{4}He a T^7 term[66], $C_7 = 11.4\,\mathrm{mJ/(mol\,K)}(T/1\,\mathrm{K})^7$, which contributes to the melting curve a T^8 term, $p_{\mathrm{MC,8}} = -(1/56)(C_7/\Delta v_{ls})T = -86\,\mathrm{Pa}\,(T/1\,\mathrm{K})^8$. The T^8 term in the melting curve, which is shown together with the roton contribution by the dashed line in Fig. 4.3, contributes $0.2\,\mathrm{Pa}$ to p_{MC} at $T = 0.46\,\mathrm{K}$, which is within the limit of our accuracy. It is also possible to estimate the possible contribution due to free vacancies from above,[3]

$$p_{\mathrm{MC,free\,vac}} = -\frac{V_s}{\Delta V_{ls}} \left(\frac{M^*}{2\pi\hbar^2} \right)^{3/2} (k_B T)^{5/2} \exp\left(-\frac{\Phi}{k_B T} \right), \qquad (4.9)$$

as their contribution cannot be detected within our accuracy. The estimated contribution $p_{\mathrm{MC,free\,vac}}$ is shown by the dash-dotted line in Fig. 4.3. The

---

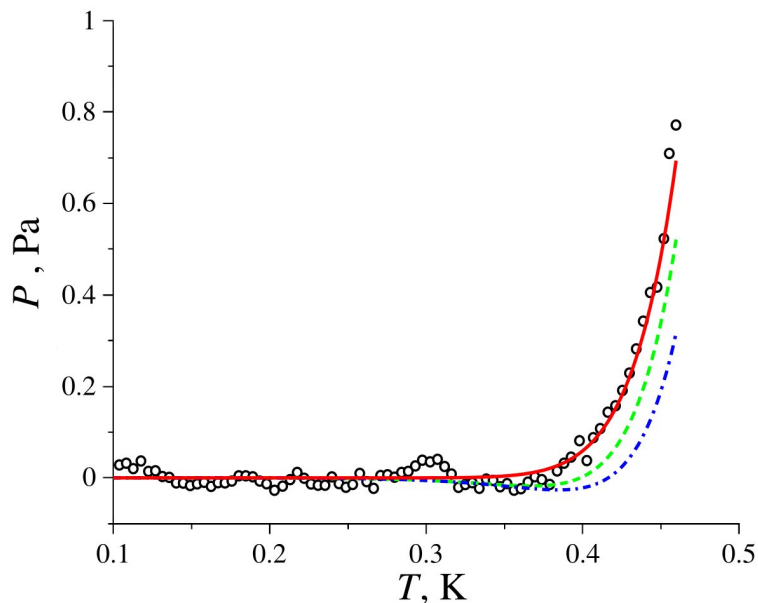[3]The minus sign in $p_{\mathrm{MC,free\,vac}}$ was missing in Paper **IX**.

Fig. 4.3 Variation of the melting pressure $p_{MC}(T) - p_{MC}(0\,K)$ of liquid ^{4}He after the T^4 term, found from the data below $0.32\,K$, has been subtracted. *Lines* show the theoretical curves due to (*solid line*) rotons, (*dashed line*) rotons and the T^8 term, and (*dash-dotted line*) rotons, T^8 term and free vacancies (see text).

lower limit for the activation energy of free vacancies can be estimated as follows. At $0.46\,K$ the contribution of vacancies is $p_{MC,freevac} = 0.2\,Pa$ (or less) and (the lower limit of) the effective mass of vacancies M^* equals to the mass of a ^{4}He atom m_4, which results in the lower limit for the activation energy $\Phi = 5.5\,K$ of free vacancies.

4.3 Thermal expansion of liquid ^{4}He

The results of the measurements on the thermal expansion coefficient a of liquid ^{4}He in the temperature range from $0.02\,K$ to $0.72\,K$ are presented in Paper **IX**. Compared to the previous measurements[69,70], our measurements shown with the solid line in Fig. 4.4 give almost by an order of magnitude smaller value for the maximum value of a near $0.5\,K$. The thermal expansion coefficient is defined as

$$a = \frac{1}{V_l}\left(\frac{\partial V_l}{\partial T}\right)_p = -\frac{1}{V_l}\left(\frac{\partial V_l}{\partial p}\right)_T \cdot \left(\frac{\partial p}{\partial T}\right)_V = \beta \cdot \left(\frac{\partial p}{\partial T}\right)_V, \qquad (4.10)$$
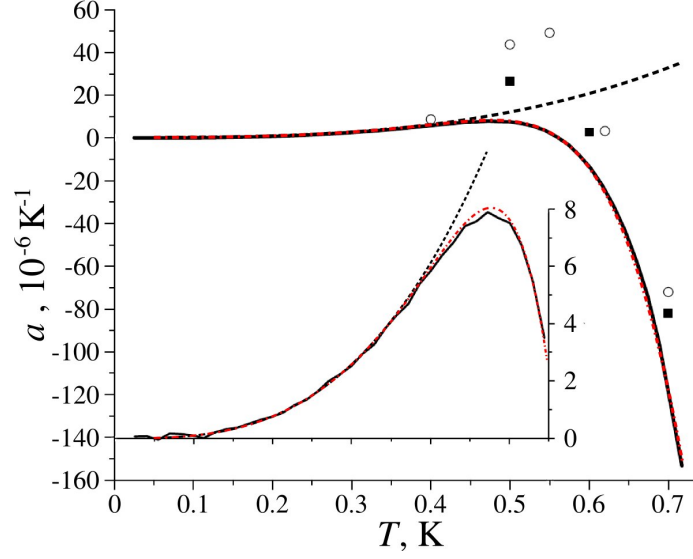
Fig. 4.4 Thermal expansion coefficient a of liquid ⁴He near the melting pressure at $2.51\,\mathrm{MPa}$. The *dashed lines* show the phonon contribution and the *dash-dotted lines* show both phonon and the roton contribution with the roton gap value of $\Delta = 7.15\,\mathrm{K}$. The fitted maximum value of $a = 8.0 \cdot 10^{-6}\,\mathrm{K}^{-1}$ is at $0.48\,\mathrm{K}$. *Circles* are from Ref.[69] and *squares* from Ref.[70]

where $\beta = -\frac{1}{V}(\frac{\partial V}{\partial p})_T$ is the isothermal compressibility of liquid. The value of a below $0.3\,\mathrm{K}$ can be explained by the contribution from phonons,

$$a_{\mathrm{ph}} = \beta(3U_0+1)\frac{S}{V} = \beta(3U_0+1)\frac{2\pi^2}{45}\frac{k_B^4}{\hbar^3 c^3}\cdot T^3 = 9.0\cdot 10^{-5}(\frac{T}{1\,\mathrm{K}})^3\,\mathrm{K}^{-1}, \quad (4.11)$$

where again $U_0 = 2.21$ and $c = 366\,\mathrm{m/s}$[71], and $\beta = \frac{1}{\rho}(\frac{\partial \rho}{\partial p})_T = 4.5\cdot 10^{-3}\,\mathrm{K}^{-1}$. The phonon contribution a_{ph} is shown with the dashed line in Fig. 4.4. Above $0.3\,\mathrm{K}$ there appears a contribution due to rotons,

$$a_{\mathrm{rot}} = \beta \cdot \left(\frac{\partial p_{L,\mathrm{rot}}}{\partial T}\right)_V, \quad (4.12)$$

which can be found out by numerically derivating $p_{L,\mathrm{rot}}$ given in equation (4.7). If the phonon contribution a_{ph} and the roton contribution a_{rot} are added together, the curves shown with the dash-dotted lines in Fig. 4.4 can be obtained using the value $7.15\,\mathrm{K}$ for the roton gap Δ.

This revised value $7.15\,\mathrm{K}$ for the roton gap Δ, obtained by fitting the full temperature dependence of a, and the revised value $6.95\,\mathrm{K}$, obtained by fitting p_l at constant volume around $25.1\,\mathrm{MPa}$, were found to be larger

than the value 6.8 K reported in Paper **IX**. The higher value 7.15 K is very close to the value 7.28 K given by Greywall measurements[72,73] and the values near 7.2 K obtained from neutron scattering experiments (see[72,73] for references).

The difference of 3% between the revised values 6.95 K and 7.15 K of Δ reflects the accuracy of the methods used to determine the roton gap. It is known that the Young modulus of the beryllium copper changes slowly in the whole temperature range and thus changes the sensitivity of the pressure gauge. It is however difficult to find out accurately how the sensitivity of the pressure gauge changes at higher temperatures due to lack of an accurate reference pressure. Even if the sensitivity of the pressure gauge was exactly known in the whole temperature range, it could be possible that the inelastic scattering processes of phonons, which result in the T^5 and T^7 terms in the specific heat of liquid ^{4}He[72,73], would become important at higher temperatures.

4.4 Stacking fault energy in ^{4}He crystals

Disorder which appears when preparing the solid ^{4}He sample has been shown to play an important role in "supersolidity"[19]. In order to understand the behavior of quantum defects, it is important to study single well-defined defects[21]. In the work described in this Thesis the stacking faults (SFs) have been studied in Paper **X**. SFs are low-energy planar defects in crystals which may appear during the crystal growth. SFs are special grain boundaries (GBs) since the plane of a SF matches the plane of a facet, and the orientations of crystals on both sides of the SF match. In hcp crystals SFs can lie only on the basal c-plane—GBs in any other orientation are high-energy defects which have the nearest neighbors severely disturbed, while the SFs have only second-nearest neighbors disturbed[33].

The process of "avalanche-like" growth of ^{4}He crystals is known to sometimes be associated with the creation of a stacking fault[35,62]. In Paper **X** it is shown that the "burst-like" creation of new atomic layers[36] might be accompanied by the creation of SFs as well, so that "avalanche-like" and "burst-like" growth can be closely related. When Rolley *et al.*[62] tried to produce high-quality crystals they found that facets may stick to the irregularities on the wall until the threshold overpressure was exceeded and the facet quickly jumped into another position.
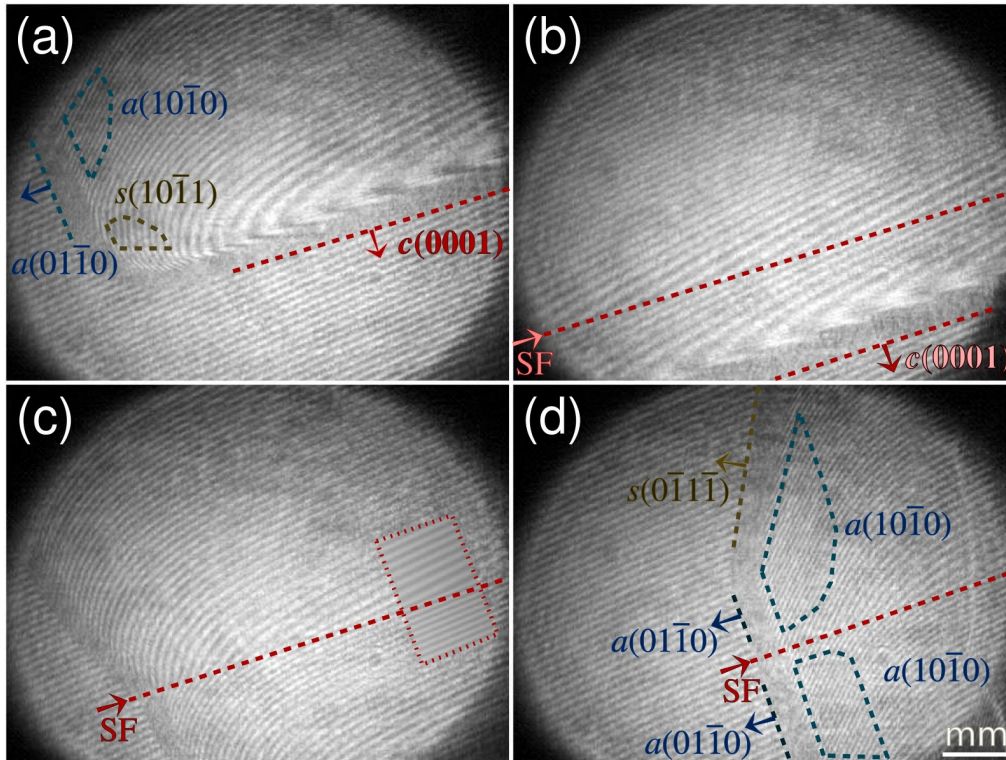
Fig. 4.5 A ^{4}He crystal at $0.2\,$K. (**a**) Immobile c-facet stays while two a-facets and the $s(10\bar{1}1)$-facet grow. (**b**) After SF has been created the c-facet continues growing. (**c**) SF is seen on the edge of the crystal. *Dotted area* has been replaced with the fitted equilibrium crystal shape. (**d**) Two a-facets grow on both sides of SF. Contact to the cell wall has stabilized the $s(0\bar{1}1\bar{1})$-facet whose size has become the largest.

The growth of the ^{4}He crystal at $0.2\,$K shown in Fig. 4.5 was studied before and after the appearance of a SF. The nearly vertical c-facet, which was immobile, touched the horizontal bottom glass of the cell and after growing for some time it touched also the vertical cell walls. From the height of the crystal it was found out that the threshold overpressure to grow c-facet and to create a SF, was $\sim 8\,$Pa, which is similar to the overpressures needed to initiate the "burst-like" growth of facets[36].

The cell walls have a major role in creating new atomic layers when the 2D nucleation of new layers or spiral growth are not effective[5]. The key role of the cell walls and similar overpressures both in "burst-like" growth and in creation of stacking faults lead to the suggestion that "burst-like" might be accompanied by the creation of stacking faults.

The role of cell walls in growing a facet in contact to the wall has been studied theoretically by Marchenko and Parshin[31] who found that at certain facet-to-wall contact angles new atomic layers may be created even without any threshold. This was later confirmed by Keshishev *et al.*[32] who found that the c-facet on ^{4}He crystals grew without any threshold when the facet-to-wall contact angle decreases below $\sim 47°$[32]. At larger contact angles the finite thresholds prevents facet growth, but the growth threshold may be weakened by the surface irregularities of the rough cell wall.

The stacking fault energy ϵ_{SF} can be measured from the shape of the groove which the SF creates on the crystal surface. The shape of the groove can be described by the Laplace-Young equation (1.1). If one of the curvatures is zero, equation (1.1) reduces to

$$(h - h_0) = -\frac{\gamma(\theta)}{\Delta\rho_{sl}} \frac{x''(h)}{[1 + x'(h)^2]^{3/2}}, \tag{4.13}$$

where θ is the angle subtended by the normal of the surface and normal of the stacking fault tilted by the angle θ_{tilt} with respect to vertical, $x'(h) = \tan(\theta - \theta_{\text{tilt}})$. The values of the anisotropic surface stiffness $\gamma(\theta)$ can be obtained from the crystallization waves experiments by Andreeva and Keshishev[24] in the range that covers the normals on the fitted surface profile, namely the range $65 < \theta < 90°$ from the [0001] orientation to the [11$\bar{2}$0] orientation. Equation (4.13) was solved numerically.

The cross section of a fitted crystal profile around the stacking fault is shown in Fig. 4.6. The area used in fitting is shown with the dotted line in Fig. 4.5(**c**). The values obtained for the contact angles were $\theta_L = 70 \pm 3°$
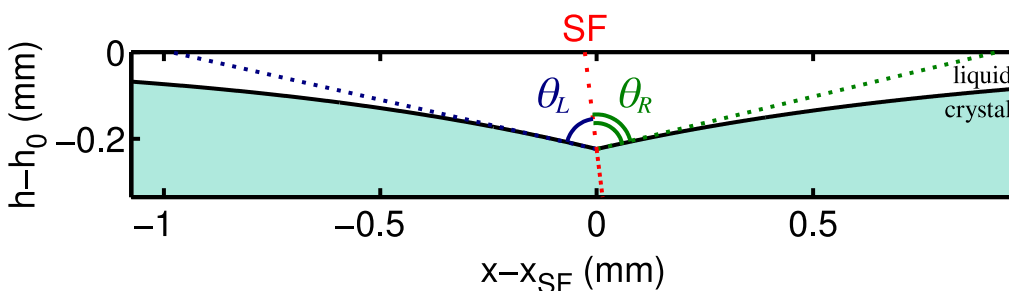

Fig. 4.6 The cross section of the fitted equilibrium crystal shape near the SF which is tilted by 7° from vertical. The dihedral angle $(\theta_L + \theta_R)$ is the sum of the contact angles θ_L and θ_R subtended by the normal of the crystal surface and the normal of the SF.

and $\theta_R = 85 \pm 3°$, which gives the dihedral angle $155 \pm 5°$. The energy of the stacking fault in the case of anisotropic surface stiffness is

$$\epsilon_{\text{SF}} = \alpha(\theta_L)\cos\theta_L + \alpha'(\theta_L)\sin\theta_L + \alpha(\theta_R)\cos\theta_R + \alpha'(\theta_R)\sin\theta_R. \quad (4.14)$$

The angular dependence of the surface tension $\alpha(\theta)$ was found out by numerically solving the differential equation (1.2) using the step energy of the (0001) facet as one of the boundary conditions, $\alpha'(0) = (\beta/a) = 14\,\mu\text{J/m}^2$, and the zero step energy condition in the $[11\bar{2}0]$ direction, $\alpha(\pi/2) = 0$. Thus, the obtained value for the surface tension $\alpha(\theta_L) = \alpha(\theta_R) = 0.18\,\text{mJ/m}^2$, and for its derivatives $\alpha'(\theta_L) = -2.8\,\mu\text{J/m}^2$ and $\alpha'(\theta_R) = 1.7\,\mu\text{J/m}^2$ resulted in the stacking fault energy $\epsilon_{\text{SF}} = (0.07 \pm 0.02)\,\text{mJ/m}^2$. The obtained value for the ϵ_{SF} is a bit smaller than the earlier estimate $0.1 - 0.2\,\text{mJ/m}^2$ based on the canyon depth $\sim 0.5\,\text{mm}$ or less[35], in our case the measured grooves on several crystals were also shallower, between $0.2 - 0.25\,\text{mm}$.

Equation (4.14) is applicable for the crystal profile only when if the orientation of the crystal is known, the groove is far from facets and one of the curvatures on the surface is negligible so that the surface can be approximated as 1D surface. Far from facets the contribution from the derivative terms α' in equation (4.14) are small, in the above example crystal about 2% or less, and without a significant loss of experimental accuracy the isotropic approximation of the SF energy can be used,

$$\epsilon_{SF} = 2\langle\alpha\rangle\cos\langle\theta\rangle. \quad (4.15)$$

On several crystals the dihedral angle of the grooves produced by SFs were found to be the same, $2\theta = 155 \pm 5°$, thus the same value $\epsilon_{\text{SF}} = (0.07 \pm 0.02)\,\text{mJ/m}^2$ was found for SFs in several crystals.

Chapter 5

Conclusions

In the 1$^{\text{st}}$ part of the work of this Thesis, the faceting of helium crystals has been studied. Around the temperature of 0.10 K where the (110) facets appear on ^{3}He crystals, the surface tension of ^{3}He crystals was found to remain nearly unchanged. At least two more types of facets were found to exist on ^{3}He crystals at 0.055 K, although more experiments should be carried out to identify them and to determine their temperature of appearance.

The quantum oscillations of the liquid-solid interface tend to dynamically roughen the crystal surface[27]. However, on the surface of ^{3}He crystals facets do appear below 0.10 K because the Fermi degeneracy of liquid ^{3}He creates a bottleneck to the spin transport through the moving interface, which dampens the oscillations of the interface. Below 0.001 K, the interface becomes localized like in classical crystals and the liquid-solid interface in ^{3}He is even more strongly pinned to the lattice than in ^{4}He, which is not obvious at all since the zero-point motion of the lighter ^{3}He atoms is larger than in ^{4}He. The antiferromagnetic ordering of nuclear spins in solid ^{3}He at 0.0009 K was not found to significantly affect the measured step energies, however, the spin currents could still strongly affect the growth of facets.

The renormalization group theory, which explains the temperature dependence of the step energy, predicts that the width of the step diverges with diminishing step energy. Thus a facet with small step energy has large step width, which could make the spiral growth more effective than the 2D nucleation of new terraces even close to the roughening temperature. Therefore, the possibility of the spiral growth should be reconsidered in the experiments on the c-facet growth[63,29] in ^{4}He crystals near 1.3 K.

Chapter V

In the 2nd part of the work of this Thesis, the melting curve of ^{4}He has been measured for normal purity ^{4}He (80 ppb of ^{3}He) and ultra-pure ^{4}He (0.3 ppb of ^{3}He) with similar results. With the accuracy of 0.1 Pa, no supersolid transition was found and the temperature dependence of the melting curve below 0.32 K can be attributed to phonons in liquid and in solid. The upper limit of the non-phonon entropy in the solid ^{4}He below 0.3 K could be set to $5 \cdot 10^{-8} R$. Thus "supersolidity" is not an intrinsic property which would change the entropy of solid ^{4}He below 0.1 K. Most probably the defects, which appear during the sample preparation and known to affect the "supersolid" fraction, are responsible for that interesting phenomenon.

The non-phonon contributions on the melting curve of ^{4}He above 0.32 K up to 0.46 K could be attributed mainly to the rotons with the gap value of 6.95 K. Other contributions, like contribution from free vacancies in solid were found to be small within the experimental accuracy of about 0.2 Pa at 0.46 K, which yielded an estimate 5.5 K for the lower limit of the activation energy of vacancies. The temperature dependence of the heat expansion coefficient a of liquid ^{4}He at 2.51 MPa could be explained with phonons and rotons with the gap value 7.15 K, which is larger than the value of the roton gap obtained from the melting curve below 0.46. The 0.2 K difference in the roton gap values reflects the accuracy of the method and is most probably due to the temperature dependence of the pressure gauge sensitivity which could be calibrated only below 0.32 K.

The energy of a stacking fault in ^{4}He, $0.07 \pm 0.02 \, \mathrm{mJ/m^2}$, was measured at 0.20 K. It would be interesting to measure the temperature dependence of the stacking fault energy and compare the results on the temperature dependence of the shear modulus of solid ^{4}He[74] which seems to follow the typical temperature dependence of the "supersolid" fraction observed in solid ^{4}He[74,10]. Some temperature dependence of the SF might be found below 0.20 K, since ultrasonic measurements[75,76,77] in hcp ^{4}He have shown that only dislocations in the basal c-plane contribute to the shear modulus by gliding in the basal plane itself[78].

References

[1] K. O. Keshishev, A. Ya. Parshin, and A. V. Babkin. *Experimental detection of crystallization waves in He^4*. Pis'ma v ZhETF **30**, 56 (1979) [JETP Lett. **30**, 63 (1979)].

[2] A. F. Andreev. *Magnetic crystallization waves in ^3He*. Physica B **210**, 378 (1995).

[3] Y. P. Feng, P. Schiffer, J. Mihalisin, and D. D. Osheroff. *Magnon thermal conductivity of solid ^3He in the U2D2 antiferromagnetic phase*. Phys. Rev. Lett. **65**, 1450 (1990).

[4] W. H. Keesom. *Solid Helium*. Communications from the Laboratory of Physics at the University of Leiden **184**, 9 (1926).

[5] S. Balibar, H. Alles, and A. Parshin. *The surface of helium crystals*. Reviews of Modern Physics **77**, 317 (2005).

[6] M. Wolfke. Ann. Acad. Sci. Techn. Varsovie **6**, 14 (1939).

[7] W. H. Keesom. *Helium*. Elsevier (New York (1942).

[8] M. W. Meisel. *Supersolid ^4He: an overview of past searches and future possibilities*. Physica B **178**, 121 (1992).

[9] G. A. Lengua and J. M. Goodkind. *Elementary excitations and a collective mode in hcp ^4He*. Journal of Low Temperature Physics **79**, 251 (1990).

[10] E. Kim and M. H. W. Chan. *Probable observation of a supersolid helium phase*. Nature **427**, 225 (2004).

[11] E. Kim and M. H. W. Chan. *Observation of Superflow in Solid Helium*. Science **305**, 1941 (2004).

[12] A. J. Leggett. *Can a Solid Be "Superfluid"?* Phys. Rev. Lett. **25**, 1543 (1970).

[13] P. Kapitza. *Viscosity of Liquid Helium below the λ-Point.* Nature **141**, 74 (1938).

[14] J. F. Allen and A. D. Misener. *Flow of Liquid Helium II.* Nature **141**, 75 (1938).

[15] A. F. Andreev and I. M. Lifshitz. *Quantum Theory of Defects in Crystals.* Zh. Eksp. Teor. Fiz. **56**, 2057 (1969) [Sov. Phys. JETP **29**, 1107 (1969)].

[16] G. V. Chester. *Speculations on Bose-Einstein Condensation and Quantum Crystals.* Phys. Rev. A **2**, 256 (1970).

[17] A. S. C. Rittner and J. D. Reppy. *Disorder and the Supersolid State of Solid ^{4}He.* Phys. Rev. Lett. **98**, 175302 (2007).

[18] E. Kim and M. H. W. Chan. *Supersolid Helium at High Pressure.* Phys. Rev. Lett. **97**, 115302 (2006).

[19] S. Balibar and F. Caupin. *Supersolidity and disorder.* Condens. Matter **20**, 173201 (2008).

[20] L. Pollet, M. Boninsegni, A. B. Kuklov, N. V. Prokof'ev, B. V. Svistunov, and M. Troyer. *Local Stress and Superfluid Properties of Solid ^{4}He.* Phys. Rev. Lett. **101**, 097202 (2008).

[21] S. Balibar. *How could a solid be superfluid?* Physics **1**, 16 (2008). doi:http://dx.doi.org/10.1103/Physics.1.16.

[22] D. Vollhardt and P. Wölfle. *The Superfluid Phases of Helium 3.* Taylor & Francis, London – New York – Philadelphia (1990).

[23] P. Nozières. *Solids Far From Equilibrium.* Cambridge University Press, Cambridge (1991). ISBN 0-521-41170-X.

[24] O. A. Andreeva and K. O. Keshishev. *Solid-Superfluid ^{4}He Interface.* Phys. Scr. **T39**, 352 (1991).

[25] D. S. Fisher and J. D. Weeks. *Shape of Crystals at Low Temperatures: Absence of Quantum Roughening.* Phys. Rev. Lett. **50**, 1077 (1983).

[26] C. Jayaprakash, W. F. Saam, and S. Teitel. *Roughening and Facet Formation in Crystals.* Phys. Rev. Lett. **50**, 2017 (1983).

[27] E. Rolley, S. Balibar, F. Gallet, F. Graner, and C. Guthmann. *The Surface Tension of b.c.c. ^{3}He Crystals.* Europhys. Lett. **8**, 523 (1989).

[28] P. Nozières and F. Gallet. *The roughening transition of crystal surfaces. I. static and dynamic renormalization theory, crystal shape and facet growth.* J. Phys. France **48**, 353 (1987).

[29] F. Gallet, S. Balibar, and E. Rolley. *The roughening transition of crystal surfaces. II. Experiments on static and dynamic propertiesnear the first roughening transition of hcp ^{4}He.* J. Phys. France **48**, 369 (1987).

[30] G. Wulff. *Zur Frage der Geschwindigkeit des Wachsthums und der Auflösung der Krystallflächen.* Z. Kristallogr. Mineral **34**, 449 (1901).

[31] V. I. Marchenko and A. Ya. Parshin. *New Possibilities in Crystal Morphology.* Pis'ma v ZhETF **83**, 485 (2006) [JETP Lett. **83**, 416 (2006)].

[32] K. O. Keshishev, V. N. Sorokin, and D. B. Shemyatikhin. *Critical behavior of the meniscus in helium crystals.* Pis'ma v ZhETF **85**, 213 (2007) [JETP Lett. **85**, 179 (2007)].

[33] W. T. Read. *Dislocations in crystals.* McGraw-Hill Book Company, Inc., New York (1953).

[34] V. Tsepelin, H. Alles, A. Babkin, R. Jochemsen, A. Ya. Parshin, and I. A. Todoshchenko. *Anisotropy of Growth Kinetics of ^{3}He Crystals below 1 mK.* Phys. Rev. Lett. **88**, 045302 (2002).

[35] A. Ya. Parshin. *Low Temperature Physics.* MIR, Moscow (1985).

[36] J. P. Ruutu, P. J. Hakonen, A. V. Babkin, A. Ya. Parshin, and G. Tvalashvili. *Growth of ^{4}He-crystals at mK-temperatures.* Journal of Low Temperature Physics **112**, 117 (1998).

[37] P. Nozières and M. Uwaha. *Low temperature mobility of the liquid-solid interface of ^{4}He.* J. Phys. France **48**, 389 (1987).

[38] R. Nomura, H. H. Hensley, T. Matsushita, and T. Mizusaki. *Crystal growth of U2D2 solid ^{3}He.* Journal of Low Temperature Physics **94**, 377 (1994).

[39] H. R. Akimoto, R. van Rooijen, A. Marchenkov, R. Jochemsen, and A. Ya. Parshin. *Crystal growth and melting velocity of spin ordered ^{3}He in 0.2 and 9 T.* Physica B **255**, 19 (2000).

[40] Y. Kawaguchi, T. Ueno, Y. Kinoshita, Y. Sasaki, and T. Mizusaki. *Crystal Growth and Mleting of Nuclear-Ordered Solid ^{3}He*. Journal of Low Temperature Physics **126**, 27 (2002).

[41] V. Tsepelin, H. Alles, A. Babkin, R. Jochemsen, A. Ya. Parshin, and I. A. Todoshchenko. *Morphology and Growth Kinetics of ^{3}He Crystals Belo 1 mK*. Journal of Low Temperature Physics **129**, 489 (2002).

[42] Y. P. Fend, P. Schiffer, D. D. Osheroff, and M. C. Cross. *Thermal boundary conductance between the U2D2 solid and B superfluid phases of ^{3}He*. Journal of Low Temperature Physics **90**, 475 (2004).

[43] F. Graner, S. Balibar, and E. Rolley. *The growth rate of ^{3}He crystals*. Journal of Low Temperature Physics **75**, 69 (1989).

[44] F. Graner, R. M. Bowley, and P. Nozières. *The growth kinetics of ^{3}He crystals*. Journal of Low Temperature Physics **80**, 113 (1990).

[45] R. L. Rusby, Durieux, M., A. L. Reesink, R. P. Hudson, Schuster, G., Köhne, M., W. E. Fogle, R. J. Soulen, and E. D. Adams. *The Provisional Low Temperature Scale from 0.9 mK to 1 K, PLTS-2000*. Journal of Low Temperature Physics **112**, 633 (2002).

[46] W. Ni, J. S. Xia, E. D. Adams, P. S. Haskins, and J. E. McKisson. *^{3}He Melting Pressure Thermometry*. Journal of Low Temperature Physics **101**, 305 (1995).

[47] P. Hariharan. *Optical Interferometry*. Academic Press Australia, Sydney (1985).

[48] J. Härme. *Multiple-Beam Interferometry and Phase Measurement of Helium Crystals*. Master's thesis, Department of Engineering Physics and Mathematics, Helsinki University of Technology (1999).

[49] J. R. Janesick. *Scientific Charge-Coupled Devices*. SPIE—The International Society for Optical Engineering, Washington (2001).

[50] V. Tsepelin, H. Alles, J. P. H. Härme, R. Jochemsen, A. Ya. Parshin, and G. Tvalashvili. *Direct Observation of (110), (100) and (211) Facets on ^{3}He Crystals*. Journal of Low Temperature Physics **121**, 695 (2000).

[51] O. A. Andreeva and K. O. Keshishev. *Identification of facets of ^{4}He crystals*. Pis'ma v ZhETF **52**, 164 (1990) [JETP Lett. **52**, 799 (1990)].
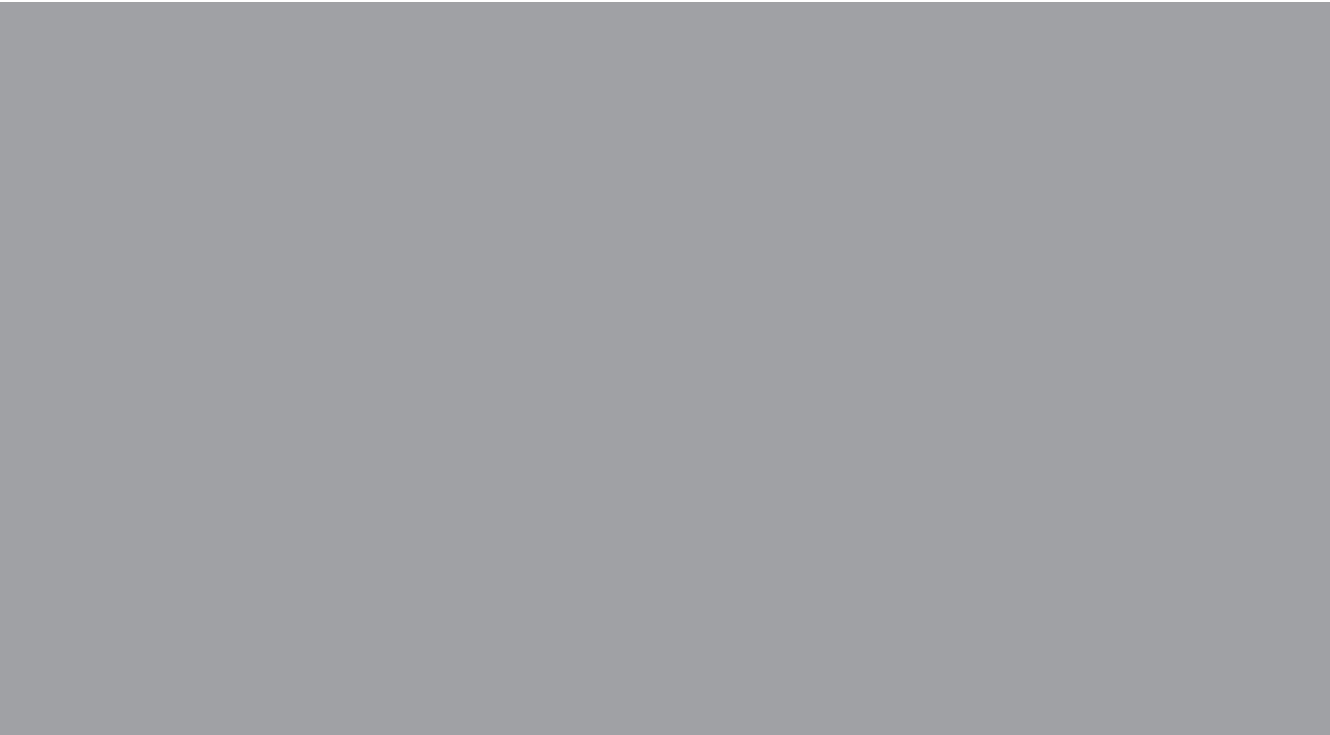
[52] R. Wagner. *The Observation of ^{3}He Crystals at Temperatures down to 1 mK Using a Cooled CCD Camera.* Ph.D. thesis, Rijksuniversiteit Leiden, Kamerlingh Onnes Laboratorium (1995).

[53] V. Tsepelin, H. Alles, A. Babkin, J. P. H. Härme, R. Jochemsen, A. Ya. Parshin, and G. Tvalashvili. *Observation of Higher Order Facets on ^{3}He Crystals.* Phys. Rev. Lett. **86**, 1042 (2001).

[54] J. S. Langer. *Instabilities and pattern formation in crystal growth.* Rev. Mod. Phys. **52**, 1 (1980).

[55] S. Balibar, C. Guthmann, and E. Rolley. *From vicinal to rough crystal surfaces.* J. Phys. I France **3**, 1475 (1993).

[56] J. Amrit and J. Bossy. *Kapitza Resistance at the Liquid-Solid Interface in ^{3}He.* Europhys. Lett. **15**, 441 (1991).

[57] W. K. Burton, F. Cabrera, and N. C. Frank. *The growth of crystals and the equilibrium structure of their surfaces.* Philos. Trans. R. Soc. A **249**, 299 (1951).

[58] L. D. Landau and E. M. Lifshitz. *Statistical Physics.* Pergamon press, New York (1980).

[59] B. Fåk and R. Scherm. *Neutron scattering studies of liquid ^{3}He and ^{3}He-^{4}He mixtures.* Physica B **197**, 206 (1994).

[60] N. V. Wellard. Ph.D. thesis, University of Manchester (1982).

[61] D. Eiszel. *Spin-independent transport parameters for superfluid ^{3}He-B.* Journal of Low Temperature Physics **54**, 427 (1984).

[62] E. Rolley, C. Guthmann, E. Chevalier, and S. Balibar. *The static and dynamic properties of vicinal surfaces on helium-4 crystals.* Journal of Low Temperature Physics **99**, 851 (1995).

[63] P. E. Wolf, F. Gallet, S. Balibar, and E. Rolley. *Crystal growth and crystal curvature near roughening transitions in hcp ^{4}He.* J. Phys. France **46**, 1987 (1985).

[64] P. G. van der Haar, C. M. C. M. van Woerkens, M. W. Meisel, and G. Frossati. *An experiment to detect vacancies and their possible Bose-Einstein condensation in solid ^{4}He.* J. Low Temp. Phys. **86**, 349 (1992).

[65] H. N. Hanson, J. E. Berthold, G. M. Seidel, and H. J. Maris. *Density of liquid ^{4}He at freezing and entropy of solid ^{4}He at low temperatures.* Phys. Rev. B **14**, 1911 (1976).

[66] W. R. Gardner, J. K. Hoer, and N. E. Phillips. *Thermodynamic Properties of ^{4}He. The hcp Phase at Low Densities.* Phys. Rev. A **7**, 1029 (1973).

[67] Y. Karaki, Y. Koike, M. Kubota, and H. Ishimoto. *Specific heat of beryllium-copper alloy at very low temperatures.* Cryogenics **37**, 171 (1997).

[68] G. W. Morley, A. Casey, C. P. Lusher, B. Cowan, J. Saunders, and J. M. Parpia. *Torsion Pendulum for the Study of Thin ^{3}He Films.* Journal of Low Temperature Physics **126**, 557 (2002).

[69] E. R. Grilly. *Pressure-volume-temperature relations in liquid and solid ^{4}He.* Journal of Low Temperature Physics **11**, 33 (1973).

[70] R. L. Mills and S. G. Sydoriak. *Thermal expansion of compressed He II.* Annals of Physics (N. Y.) **34**, 276 (1965).

[71] B. M. Abraham, Y. Eckstein, J. B. Ketterson, M. Kuchnir, and P. R. Roach. *Velocity of Sound, Density, and Grüneisen Constanst in Liquid ^{4}He.* Phys. Rev. A **1**, 250 (1970).

[72] D. S. Greywall. *Specific heat and phonon dispersion of liquid ^{4}He.* Phys. Rev. B **18**, 2127 (1978).

[73] D. S. Greywall. *Erratum: Specific heat and phonon dispersion of liquid ^{4}He.* Phys. Rev. B **21**, 1329 (1980).

[74] D. James and J. Beamish. *Low-temperature shear modulus changes in solid ^{4}He and connection to supersolidity.* Nature **450**, 853 (2007).

[75] Y. Hiki and F. Tsuruoka. *Ultrasonic Attenuation in HCP ^{4}He crystals.* Phys. Lett. A **56**, 484 (1975).

[76] Y. Hiki and F. Tsuruoka. *Dislocation damping in HCP ^{4}He crystals.* Phys. Lett. A **62**, 50 (1977).

[77] F. Tsuruoka and Y. Hiki. *Ultrasonic attenuation and dislocation damping in helium crystals.* Phys. Rev. B **20**, 2702 (1979).

[78] M. A. Paalanen, D. J. Bishop, and H. W. Dail. *Dislocation Motion in hcp ^{4}He.* Phys. Rev. Lett. **46**, 664 (1981).

Abstracts of publications

I   The surface tension ^{3}He crystals is measured at 77–110 mK. The surface tension was measured on slowly melting crystals in order to avoid appearance of facets below 100 mK. Within the accuracy no increase of the surface tension was found near the roughening transition temperature temperature, thus the appearance of facets is not related to the change in the value of the surface tension but rather in the enhanced interface-to-lattice coupling.

II   The faceting of bcc ^{3}He crystals is studied optically. Using our interferometric technique we found at least three types of facets to be present on ^{3}He crystals up to 55 mK, while previously only the (110) facet has been observed at such high temperatures.

III   The temperature dependence of the step energy of (110) facet on ^{3}He crystals is measured at 60–110 mK using the imaged crystal surface as a highly sensitive overpressure gauge. The obtained step free energies show that the interface-to-lattice coupling is very weak at these temperatures, which is shown to be due to quantum fluctuations of the interface. The appearance of the facets on ^{3}He crystals at 100 mK, which is well below the roughening temperature of 260 mK, can be shown with the renormalization group approach to be due to the increased interface-to-lattice coupling as the quantum fluctuations of the interface become dampened at lower temperatures due to the Fermi degeneracy of liquid ^{3}He. Consequently, at very low temperatures the interface-to-lattice coupling is nearly strong.

IV   The subject of Paper **III**, which describes the measurements on the step energy of (110) facet on ^{3}He crystals at 60–110 mK, is gone deeper and in addition the elaboration and transport of heat during the crystal growth is discussed. The growth of rough surface was found to be limited by the transport of the latent heat of crystallization, which is in accordance with theoretical predictions and previous measurements near the melting curve minimum of ^{3}He. The mobility of an elementary step was found also to be limited by the latent heat.

V   A new method is applied on slowly melting ^{3}He crystals to measure the step energies from the critical size of collapsing facets. The step energies were obtained for the (110) and (100) facets on ^{3}He crystals near 1 mK. It was found that the antiferromagnetic transition in solid ^{3}He at 0.902 mK has no significant effect on the step energy.

VI A remark is made on the earlier careful studies on the roughening of ^{4}He in Paris in 1980s. In the roughening theory which is used to explain the measured temperature dependence of the step energy of c-facet on ^{4}He crystals, the step width diverges with decreasing step energy when the temperature approaches the roughening temperature. Consequently, with the step energies they measured near the roughening temperature assuming 2D nucleation of atomic terraces, an another mechanism provided by screw dislocations should be more effective than 2D nucleation.

VII The melting curve of normal purity ^{4}He is measured at 10–400 mK in order to see a heat capacity signature of a possible supersolid transition of the solid ^{4}He. Within the accuracy of 0.05 Pa the experimental data can be explained by the sound velocity in liquid ^{4}He and the Debye temperature of solid ^{4}He. Only below 80 mK we found a deviation of ~ 0.5 Pa from the T^4 dependence, but that deviation could not be attributed to the possible supersolid transition.

VIII With high-purity ^{4}He (containing 0.3 ppb of ^{3}He impurities) and additional optical observations on the ^{4}He crystals, the melting curve of ^{4}He is demonstrated to follow the expected T^4 dependence due to phonons within 0.05 Pa in temperature range from 10 to 320 mK. The low temperature deviation found in Paper **VII** could be eliminated through a recalibration of the sensitivity of the BeCu pressure gauge. With high-quality ^{4}He crystals the non-phonon entropy which contributes to the melting curve are thus smaller than $\sim 5 \cdot 10^{-8} R$.

IX The melting curve is measured up to 0.45 K and the heat expansion of liquid ^{4}He is studied at constant volume up to 0.72 K. Below 0.32 K, the phonons in liquid ^{4}He and in solid ^{4}He were responsible of the T^4 dependence of both the melting curve and the heat expansion of liquid. Above 0.32 K the rotons in liquid started to contribute in liquid ^{4}He, and the deviation from the T^4 dependence in heat expansion of the liquid resulted in the roton gap value of 6.8 K.

X The appearance and the energy of the stacking faults is studied in hcp ^{4}He crystals. A connection was found between the appearance of a stacking fault and the initiation of a burst-like creation of new atomic layers on ^{4}He crystals. The stacking fault was found to create a groove on the crystal surface with the dihedral angle of $155\pm5°$. The measured stacking fault energy was found to be about 0.4 of the surface tension of the liquid-solid interface of ^{4}He.